Testing of Microchannels and Lab-Grown Stress Corrosion Cracks for Quantification of Aerosol Transmission

Spent Fuel and Waste Disposition

Prepared for
US Department of Energy
Spent Fuel and Waste Science and Technology

P. G. Jones, D. G. Fascitelli, A. G. Perales and S. G. Durbin
Sandia National Laboratories

August 25, 2023
Milestone No. M2SF-23SN010207065
SAND2023-#### R

DISCLAIMER

This information was prepared as an account of work sponsored by an agency of the U.S. Government. Neither the U.S. Government nor any agency thereof, nor any of their employees, makes any warranty, expressed or implied, or assumes any legal liability or responsibility for the accuracy, completeness, or usefulness, of any information, apparatus, product, or process disclosed, or represents that its use would not infringe privately owned rights. References herein to any specific commercial product, process, or service by trade name, trade mark, manufacturer, or otherwise, does not necessarily constitute or imply its endorsement, recommendation, or favoring by the U.S. Government or any agency thereof. The views and opinions of authors expressed herein do not necessarily state or reflect those of the U.S. Government or any agency thereof.

Prepared by
Sandia National Laboratories
Albuquerque, New Mexico 87185 and Livermore, California 94550

Sandia National Laboratories is a multimission laboratory managed and operated by National Technology & Engineering Solutions of Sandia, LLC, a wholly owned subsidiary of Honeywell International, Inc., for the U.S. Department of Energy's National Nuclear Security Administration under contract DE-NA0003525.

ABSTRACT

The formation of a stress corrosion crack (SCC) in the canister wall of a dry cask storage system (DCSS) has been identified as a potential issue for the long-term storage of spent nuclear fuel. The presence of an SCC in a storage system could represent a through-wall flow path from the canister interior to the environment. Modern, vertical DCSSs are of particular interest due to the commercial practice of using higher backfill pressures in the canister, up to approximately 800 kPa, compared to their horizontal counterparts. This pressure differential offers a relatively high driving potential for blowdown of any particulates that might be present in the canister. In this study, the rates of gas flow and aerosol transmission of a spent fuel surrogate through an engineered microchannel with dimensions representative of an SCC were evaluated experimentally using coupled mass flow and aerosol analyzers. The microchannel was formed by mating two gage blocks with a linearly tapering slot orifice nominally 13 μm (0.005 in.) tall on the upstream side and 25 μm (0.0010 in.) tall on the downstream side. The orifice is 12.7 mm (0.500 in.) wide by 8.86 mm (0.349 in.) long (flow length). Surrogate aerosols of cerium oxide, CeO_2, were seeded and mixed with either helium or air inside a pressurized tank. The aerosol characteristics were measured immediately upstream and downstream of the simulated SCC at elevated and ambient pressures, respectively. These data sets are intended to add to previous testing that characterized SCCs under well-controlled boundary conditions through the inclusion of testing improvements that establish initial conditions in a more consistent way. While the engineered microchannel has dimensions similar to actual SCCs, it does not reproduce the tortuous path the aerosol-laden flow would have to traverse for eventual transmission. SCCs can be rapidly grown in a laboratory setting given the right conditions, and initial characterization and clean-flow testing has begun on lab-grown crack samples provided to Sandia National Laboratories (SNL). Many such samples are required to produce statistically relevant transmission results, and SNL is developing a procedure to produce samples in welded steel plates. These ongoing testing efforts are focused on understanding the evolution in both size and quantity of a hypothetical release of aerosolized spent fuel particles from failed fuel to the canister interior and ultimately through an SCC.

This page is intentionally left blank.

ACKNOWLEDGEMENTS

This work was funded by the U.S. Department of Energy (DOE), Office of Nuclear Energy Spent Fuel and Waste Disposition Research and Development Program.

The authors would like to express their appreciation to Ned Larson of the DOE for his programmatic leadership and vision. The technologist team of Adrian Perales, Thad Vice, and Greg Koenig are commended for their tireless efforts and attention to detail in making this work possible. The authors would also like to thank Jonathan Tatman and his team at the Electric Power Research Institute for the lab-grown crack samples. The collaboration with Charles Bryan, Andrew Knight, and Tyler McCready on producing lab-grown stress corrosion cracks at Sandia National Laboratories is appreciated as well.

This page is intentionally left blank.

CONTENTS

LIST OF FIGURES

This page is intentionally left blank.

LIST OF TABLES

This page is intentionally left blank.

EXECUTIVE SUMMARY

A potential through-wall stress corrosion crack (SCC) in the canister of a dry cask storage system (DCSS) could create a flow path from the canister interior to the environment. Because of the backfill pressures of modern DCSSs up to 800 kPa, this pressure differential offers a relatively high driving potential for blowdown of any particulates that might be present in the canister. This study seeks to simulate the key physics for aerosol transmission through geometries and conditions approaching those expected for an SCC in a storage canister.

In this report, gas flow and mass transmission of surrogate spent fuel particulates (CeO_2) are measured upstream and downstream of an engineered microchannel. The microchannel, shown in Figure E.1, has dimensions representative of an SCC. Mass flow rate of the carrier gas and transmission of the particulate was evaluated experimentally using coupled mass flow and aerosol analyzers. This simplified geometry lacks the tortuosity and surface roughness characteristic of real SCCs but offers well defined and repeatable conditions to gain insight into the hypothetical release fraction from a canister to the environment. Figure E.2 shows a compilation of transmission fraction data as a function of particulate mass median diameter (MMD). As expected, smaller particle size distributions as given by smaller MMD are more efficient passing through the microchannel as compared to larger particle size distributions.

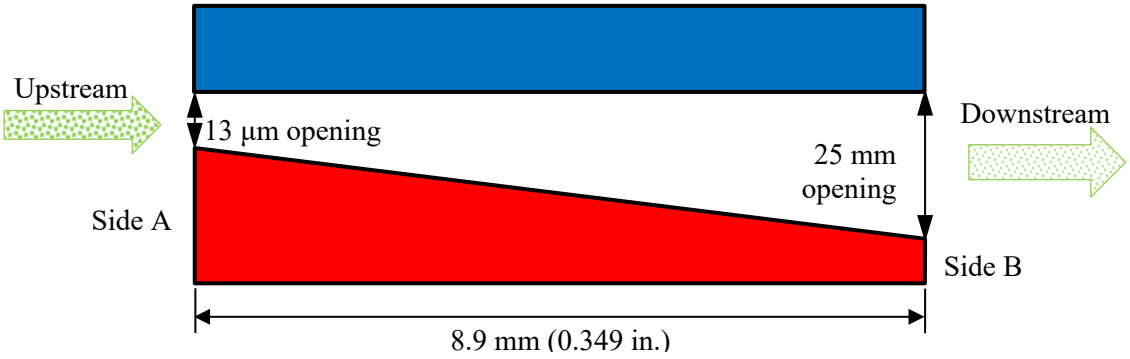

Figure E.1 Illustration of the linear slot microchannel (not to scale).

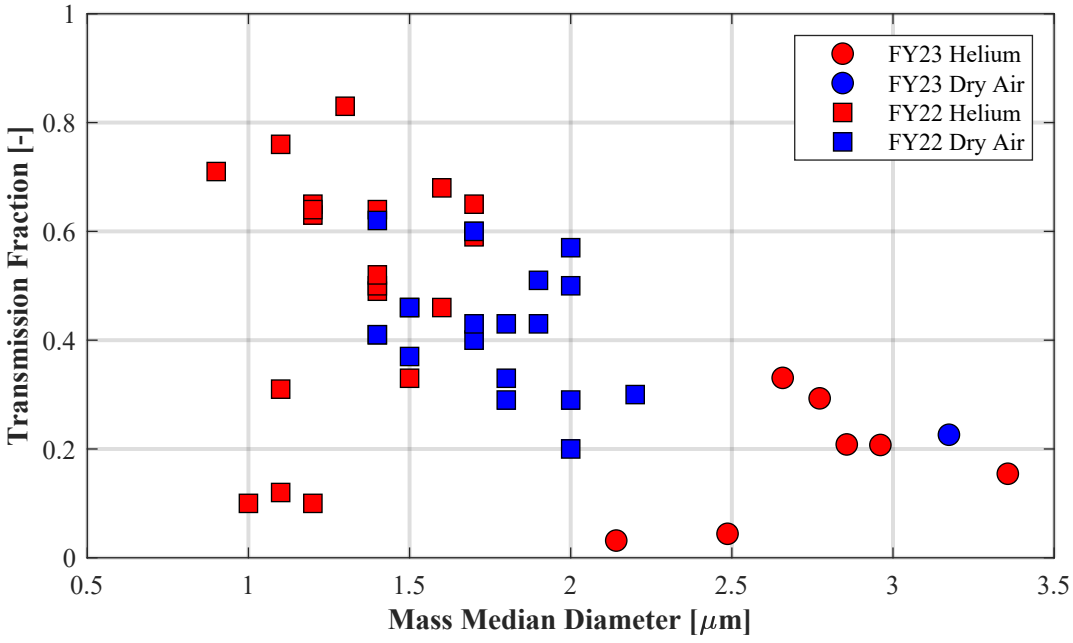

Figure E.2 Compilation of surrogate spent fuel transmission through a microchannel as a function of MMD.

While microchannels are advantageous for testing because they are easily serviceable and reusable, they lack certain characteristics of actual SCCs such as tortuosity and interior roughness. SCCs can be grown at an accelerated rate in a laboratory setting given adequate tensile stress is developed in a specimen and the specimen is exposed to a sufficiently corrosive species. The Electric Power Research Institute (EPRI) provided two lab-grown crack samples for aerosol transmission testing at Sandia National Laboratories (SNL). Preliminary flow tests without the presence of aerosols were conducted with the lab-grown crack samples. As the lab-grown cracks will foul with aerosol after a single use, SNL is developing a technique to produce lab-grown crack samples for future aerosol transmission testing and progress is reported in this report as well.

ACRONYMS

AED	aerodynamic equivalent diameter
alpm	actual liters per minute
CDF	cumulative distribution function
CT-scan	computed tomography scan
DCSS	dry cask storage system
DOE	US Department of Energy
EDM	electrical discharge machining
EPRI	Electric Power Research Institute
FS	full scale
GSD	geometric standard deviation
HEPA	high-efficiency particulate absorbing
MMD	mass median diameter
NE	Nuclear Energy
ORNL	Oak Ridge National Laboratory
PDF	probability distribution function
PNNL	Pacific Northwest National Laboratory
PWR	pressurized water reactor
RBG	rotating brush generator
SCC	stress corrosion crack
SFWD	Spent Fuel and Waste Disposition
slpm	standard liters per minute
SNF	spent nuclear fuel
SNL	Sandia National Laboratories
STP	standard temperature and pressure

This page is intentionally left blank.

TESTING OF MICROCHANNELS AND LAB-GROWN STRESS CORROSION CRACKS FOR QUANTIFICATION OF AEROSOL TRANSMISSION

This report fulfills milestone M2SF-23SN010207065 in the Aerosol Source Term work package (SF-23SN01020706). This work was sponsored under the Department of Energy's (DOE) Office of Nuclear Energy (NE) Spent Fuel and Waste Disposition (SFWD) campaign.

1 INTRODUCTION

Dry cask storage systems (DCSSs) for spent nuclear fuel (SNF) are designed to provide a confinement barrier that prevents the release of radioactive material, maintains SNF in an inert environment, provides radiation shielding, and maintains subcriticality conditions. Dry storage canisters are backfilled with an inert gas, typically helium, to maintain a stable environment and increase thermal conductivity within the canister. Backfill pressures in a vertical DCSS typically reach up to 800 kPa. SNF is initially stored in pools of water for cooling where the water also provides radiation shielding. As these pools get closer to capacity, dry storage systems are becoming the primary means of extended storage. After sufficient cooling in pools, SNF is loaded into a canister and placed inside a storage cask, where the canister is welded shut. The DCSS is then decontaminated and dried, and the system is moved to an on-site dry storage location. Figure 1.1 shows the major components of a DCSS for SNF.

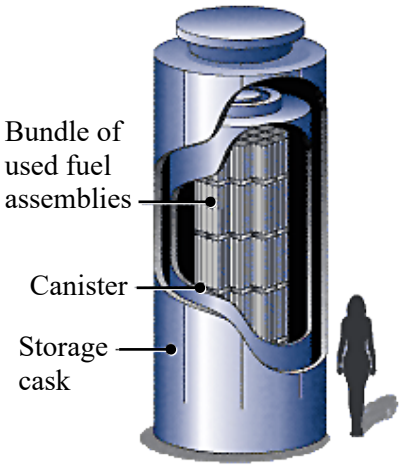

Source: https://www.nrc.gov/waste/spent-fuel-storage/diagram-typical-dry-cask-system.html

Figure 1.1 Typical dry cask storage system.

Typically, the canisters are made of stainless steel. The dry storage system is designed with an open volume between the canister and the storage cask. Rejection of the decay heat is accomplished by air flowing from air inlets at the bottom of the cask to outlets at the top via natural convection. This passively cooled design also allows dust from the environment into the system. These particulates may then collect on the surfaces of the canister. As the SNF cools, salts contained in the dust may deliquesce in the presence of moisture from the ambient relative humidity to form concentrated brines, which may contain corrosive species such as chlorides. These species can cause localized corrosion, called pitting. With sufficient stresses, these pits can evolve into stress corrosion cracks (SCCs), which could penetrate through the canister wall and allow communication from the interior of the canister to the external environment [Schindelholz, 2017].

1.1 Objective

The purpose of this on-going research is to explore the characterization of aerosols in DCSSs that have developed a through-wall SCC. The characteristics of interest include particulate suspension, transport, depletion, and transfer/deposition in the SCC.

This testing employed engineered slots with characteristic dimensions similar to those in SCCs as analogs. A diverging crack geometry was explored in FY21 and iterated with more scrutiny in this testing to better approximate SCCs. Additionally, efforts have been made to move beyond the use of engineered microchannels to testing of actual SCCs that were rapidly grown in a laboratory setting, which are thought to be highly representative of SCCs in dual purpose canisters (DPC).

A Palas Promo 3000 HP high resolution aerosol spectrometer has been integrated into the experimental system that can directly monitor aerosol samples at elevated pressures. This high-pressure aerosol characterization system is designed to opto-mechanically switch between monitoring upstream and downstream sensing detector elements offering nearly simultaneous real-time measurements and eliminating the instrument bias seen in previous testing [Durbin *et al.*, 2018]. This test apparatus has consistently demonstrated a flexible technological approach to directly measure aerosol transmission through the engineered microchannel/slot at conditions of interest.

1.2 Previous Studies

The data obtainable from the measurement of particulate segregation in flows through open channels has significance in multiple fields. Studies include particle penetration through building cracks [Lewis, 1995, Liu and Nazaroff, 2003, Mosley *et al.*, 2001] to nuclear reactor safety [Powers, 2009], and more recently, storage and transportation of SNF in dry casks [Durbin *et al*., 2020 & 2021, Jones *et al*., 2022]. Studies of these systems contribute to the understanding of particulate segregation through small channels as functions of particle size and concentration, channel dimensions, and differential pressures.

Previous work has contributed to the characterization of particulate segregation across channel flow for a range of particle sizes in aerosols. Lewis [Lewis, 1995] was motivated by a lack of empirical studies to support the development of protection factors against solid particles for enclosures. This protection factor was taken as the ratio of the dose of an outside concentration of particulates to the dose accumulated inside an enclosure for a specified time, with the doses defined as concentration-time integrals. Models were derived describing the total transport fraction of particles across a rectangular slot into an enclosure as functions of particle size, differential pressures, and slot heights. Lewis described an experimental apparatus with synthesized aerosols (containing either talc, aluminum oxide, titanium oxide, various silica powders, or ambient dust) mixed in a chamber containing an enclosure with a rectangular slot open to the chamber. A differential pressure was established between the chamber and the enclosure. Protection factors were found by comparing mass concentration values inside and outside the enclosure over a given time. The primary observations here were the decrease in total transport fraction with increasing particle size from 1-10 μm as well as a decrease in protection factor (corresponding to an increase in total transport fraction) with increasing differential pressures and slot heights.

Liu and Nazaroff [Liu and Nazaroff, 2003] conducted experiments of aerosol flow through rectangular slots using various building materials, including aluminum, brick, concrete, and wood. The slot heights were 0.25 mm and 1 mm, which are large compared to the micron- to submicron-sized particles they flowed through the cracks. They obtained data for particle penetration (defined as the ratio of downstream to upstream particle concentration), related to total transport fraction, as a function of particle size. They found that, for 0.25 mm cracks, particle sizes between 0.1-1 μm achieved penetration factors near unity, while smaller and larger particles showed diminished penetration factors for pressure differentials of 4 and 10 Pa. Meanwhile, for 1 mm slot heights, the penetration factors were near unity for the majority of the particle size distribution. Their results matched closely with models they created from analysis of

particle penetration through simplified cracks [Liu and Nazaroff, 2001] and had similar qualitative conclusions to Lewis's work.

Mosley studied particle penetration through a 0.508 mm slot height between aluminum plates with particles of aerodynamic equivalent diameters (AEDs) from 0.1 to 5 µm [Mosley *et al.*, 2001]. They found penetration factors close to unity for particle sizes between 0.1-1 µm, with a sharp drop-off in penetration factor for particle sizes larger than 1 µm for pressure differentials between 2 and 20 Pa – this was consistent with Liu and Nazaroff's results when considering the order of magnitude of the pressure differentials and particle size distributions.

The motivation behind the above work was based on ambient particle penetration of enclosures and the number of particles subject to human exposure, with slot heights and pressure differentials corresponding to conditions typically associated with building cracks and pressure differences between indoor and outdoor environments, respectively.

Casella studied the flow from pinhole breaches and particle deposition inside the breach for canisters with moderate pressure backfills [Casella *et al.*, 2006, Casella *et al.*, 2007]. The pinholes examined in these studies were relatively small, with diameters on the order of 10 µm. The particulates considered were also relatively small, with diameters of 0.05 to 0.1 µm. The initial, internal canister backfill pressure was 188 kPa. These analytic studies demonstrated that the effect of channel plugging can greatly reduce the leak rate from a canister.

However, the channel dimensions considered do not apply to the channel geometry associated with SCCs from potential corrosion of dry casks. The literature reports typical crack heights to be around 16 to 30 µm [EPRI, 2014 & 2017; Meyer *et al.*, 2016] and internal pressures of 100 to 760 kPa (14.5 to 110 psig) [EPRI, 2017] for a range of cask models. Therefore, an apparatus and procedures were developed to investigate a slot height on the order of 10 µm and pressure differentials on the order of 100 kPa to supplement the established database of particulate transmission in microchannel flows. This experimental approach has demonstrated adaptability for future testing of more prototypic stress corrosion crack geometries. Preliminary results using air as the carrier gas indicated 44% of the aerosols available for transmission were retained upstream of the microchannel [Durbin *et al.*, 2018].

1.3 Current Study and Collaborative Modeling

1.3.1 Uniqueness of Current Study

An aerosol spectrometer is utilized for this study to measure the size resolved aerosol concentration, also known as aerosol size distribution. The Palas Promo 3000 HP is fiber-optically coupled to two Welas 2200 high pressure aerosol sensors. The high-pressure aerosol sensor directly samples gas streams at native pressures up to 1.0 MPa. Rapid fiber optic switching allows a single instrument to analyze the upstream and downstream aerosol sensors in quasi-simultaneous fashion using the same optical detector. Switching of upstream and downstream sensors occurred every 60 seconds (see Section 2.4.4 for details). Thus, instrument bias was eliminated, and sample line losses were substantially minimized.

This study is a continuation from previous microchannel aerosol transport testing at Sandia National Laboratories (SNL) [Jones *et al*., 2022] and is conducted on the same microchannel which varies in depth linearly from 13 to 25 µm (detailed in Section 2.2). The key difference in this work is the use of a high pressure rotating brush generator (RBG) which allows for active seeding of aerosols into the pressure vessel through the duration of the test. While an actual DPC would not have a constant supply of aerosol for transport through a SCC, tighter control of upstream conditions will hopefully allow for greater understanding of the phenomena of aerosol transport through these types of cracks. The results of the refinements explored in FY23 are presented here.

The aerosol transmission through the linearly varying microchannel orifice was measured while actively seeding aerosols into a tank kept at constant pressure containing helium. A best attempt is made to also

maintain consistent aerosol concentration and size distribution across all tests which proved difficult to achieve. Despite the somewhat chaotic nature of aerosols and difficulties in testing, this methodology achieved more uniform upstream conditions with the distribution consisting of larger particles than achieved previously.

This study also continues the progression to more prototypic crack geometry in moving from the uniform slot orifice explored previously [Durbin *et al*., 2020] and the linearly diverging geometry [Durbin *et al*., 2021 and Jones *et al*., 2022], to highly prototypic lab-grown SCCs. Clean flow testing of cracks provided by the Electric Power Research Institute (EPRI) using air and helium was conducted and flow rate as a function of pressure drop is presented in this work. The cracks will be subsequently tested using aerosols. Only two such samples were provided, so SNL is developing their own procedure to rapidly grow cracks under controlled laboratory conditions.

1.3.2 Collaborative Modeling Efforts

Modeling efforts from Pacific Northwest National Laboratory (PNNL) and Oak Ridge National Laboratory (ORNL) in collaboration with Purdue University are being conducted in parallel to the modeling and experimental efforts from SNL. The focus of these efforts can be localized to three different areas as illustrated in Figure 1.2.

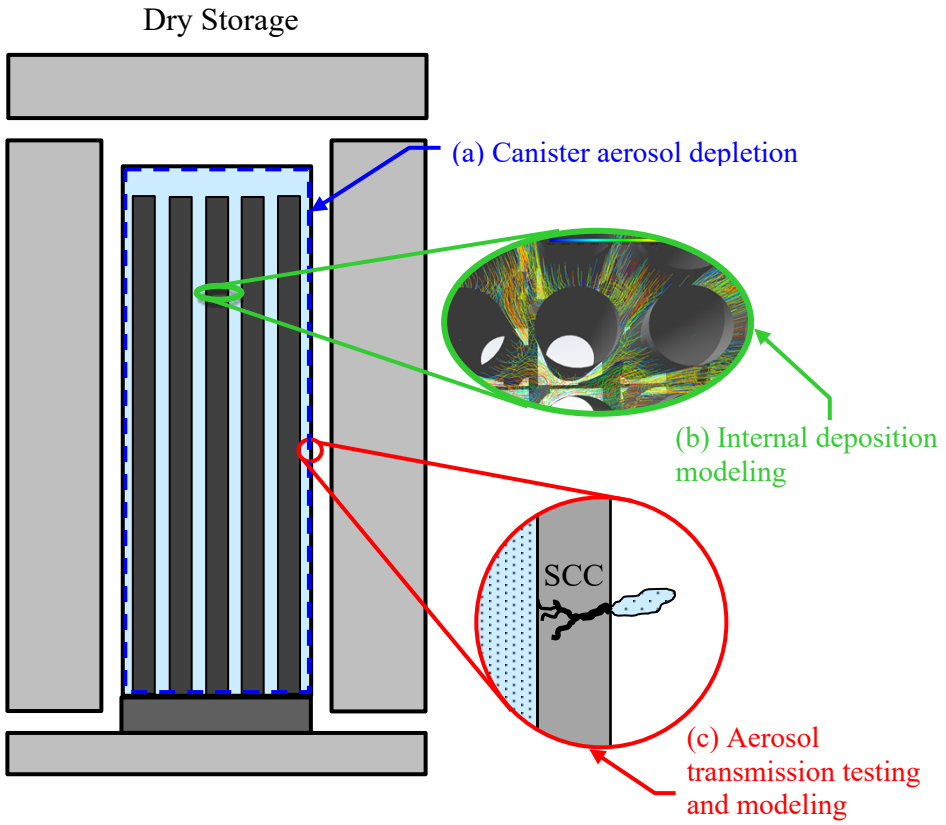

Figure 1.2 Collaborative modeling and testing areas.

GOTHIC modeling at PNNL [Lanza *et al*., 2021, Lanza *et al*., 2022] and MELCOR modeling by Phillips and Gelbard at SNL [Phillips and Gelbard, 2021, Phillips, 2022] focus on aerosol depletion within the canister internal volume (Figure 1.2(*a*)). Gelbard and Durbin at SNL [Gelbard and Durbin, 2023] investigate aerosol deposition on spacer grids using the computation fluid dynamics code Fluent (Figure

1.2(*b*)). First principles modeling of aerosol transport/depletion in microchannels by Chatzidakis at Purdue University and Sasikumar at ORNL [Chatzidakis and Sasikumar, 2021] as well as the experimental study presented in this report focus separately on aerosol transmission through a stress corrosion crack (Figure 1.2(*c*)). The modeling and experimental efforts running in parallel across multiple national laboratories will serve to develop further understanding of aerosol transport phenomena in DCSSs and SCCs.

This page is intentionally left blank.

2 APPARATUS AND PROCEDURES

The experimental approach adopted for these studies is similar to previous studies [Lewis, 1995; Mosley *et al.*, 2001; Liu and Nazaroff, 2001 and 2003] in that aerosol analyzers are used to characterize the particle size distribution and concentration present in the gas before and after flowing through a simulated crack. Because these previous studies considered aerosol transport through building walls or containment structures, the focus was on flows through relatively wide and long slots driven by constant low pressure drops. In the present study, consideration was given to aerosol transport through dry storage canister walls. Here, the focus was on much narrower and shorter microchannels that represent stress corrosion cracks through the canister wall with aerosol transport driven by initially higher pressure drops across the wall.

FY22 introduced constant pressure testing to decouple the pressure transient which allowed better examination of the SCC discharge characteristics as it was fouled with deposited particulates. FY23 introduces active seeding of aerosols into the pressure tank to decouple the depletion of aerosols in the tank which preferentially affects larger heavier particles and alters both the overall aerosol concentration and size distribution.

Future efforts will involve aerosol flow testing of lab-grown SCCs. In developing that testing capability, a new test section has been fabricated and installed in a way to bypass the storage tank which is contaminated with aerosols. This bypass section, described at the end of Section 2.1, has been used to conduct clean flow testing of lab-grown cracks without the presence of particulates which are described in Section 2.3

2.1 General Construction and Operation

The general layout of the experimental setup is illustrated in Figure 2.1 and Figure 2.2. A 0.908 m^3 (240 gal) pressure tank is used to simulate the canister. Several stirring fans were installed roughly along the tank centerline to stir the particulates and minimize aerosol depletion through deposition of particles on the inner surface of the tank over the course of a test. The tank was pressurized to the desired pressure for a given test. A Palas RBG, see section 2.4.5, was used to seed the tank up to a concentration of approximately 1.6 x 10^4 particles/cm^3. Additional details on the desired and actual initial aerosol concentrations are discussed in Section 2.5.2. A Palas Promo 3000 HP spectrometer and Welas 2200 high pressure aerosol sensor, described in Section 2.4.4, were used to monitor the aerosol concentration in the tank, and the RBG settings (flow rate, brush speed, piston speed) were adjusted to achieve a relatively constant aerosol concentration and size distribution in the tank. Clean helium to the RBG was supplied by an external flow controller and a back pressure controller was used to release helium from the tank to maintain constant tank pressure prior to and for the duration of the test.

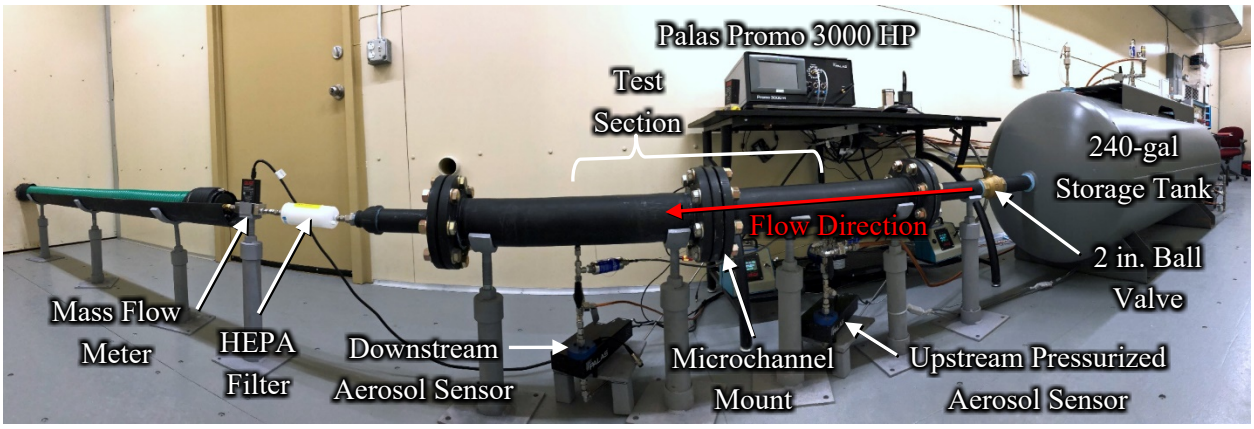

Figure 2.1 General layout of the experimental apparatus.

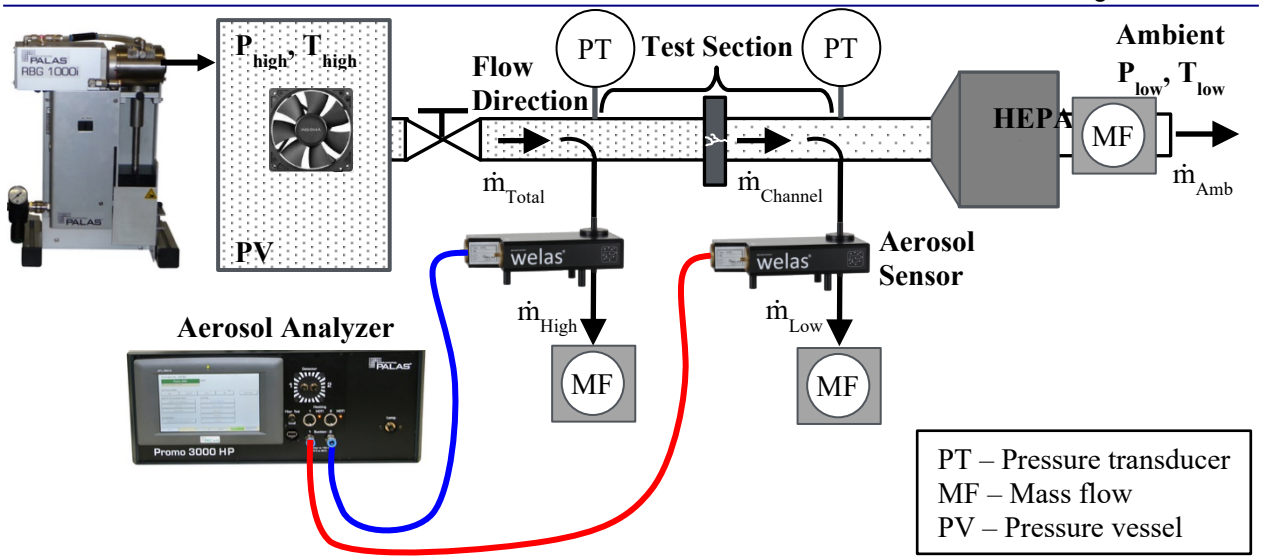

Figure 2.2 Schematic of the experimental apparatus showing the major components.

Tests were initiated by opening the 2-inch ball valve to release the particle laden flow into the test section. Prior to test initiation, clean helium was used to displace ambient air out of the upstream and downstream portions of the test section. Gas flow exhausts to ambient either through the mass flow meter at the end of the test section, or through the aerosol sensors and associated mass flow controllers. The engineered microchannel, containing an SCC-like geometry, was mounted in the middle of the test section comprised of mounting flanges and two 0.61 m (24 in.) long, 0.10 m (4 in.) diameter schedule 40 pipe nipples (see Figure 2.2). A sample stream was drawn from the centerline at the nipple midpoint (0.30 m from the microchannel) on the high-pressure upstream and low-pressure downstream sides of the test microchannel. Smooth bend 90° fittings are installed inside the pipe nipples with the inlet facing the flow and serves as the sample line for the aerosol sensors.

An identical Palas Promo 3000 HP analyzer connected to two Welas 2200 high pressure aerosol sensors were used to characterize the aerosol concentration and size distribution in the upstream and downstream portions of the test section. Flow controllers metered the sample flow through each of the aerosol sensors at a constant rate of 0.5 actual liters per minute (alpm). In cases where the flow required for the downstream Welas sensor was greater than the flow through the crack, a cover gas was used so that ambient air was not drawn from the exhaust portion of the test section through the sensor. Gas flow from the tank and through the test section was measured by a mass flow meter downstream of the test section. Pressure transducers monitor the upstream and downstream sides of the microchannel, the tank, and ambient pressures. Thermocouples were also installed at the same locations. A low pressure drop, high-efficiency particulate absorbing (HEPA) filter was used to remove all aerosols from the exhaust stream before the final mass flow measurement.

The newly fabricated test section used for testing of lab-grown cracks is shown in Figure 2.3 and is designed to be directly swapped with the test section called out in Figure 2.1. The upstream and downstream sections are fabricated from two 0.61 m (24 in.) long, 0.10 m (4 in.) diameter schedule 40 SS pipe nipples welded to mounting flanges. The lab-grown crack sample, which has a unique bolt pattern, bolts directly to the upstream and downstream sections. To evaluate the pressure drop across the crack without fouling the crack with aerosols from the tank, the lab-grown crack test section was installed in a manner which bypasses the aerosol tank. A pressure controller was used to step the upstream pressure from ambient to 800 kPa at various intervals. The procedure started at ambient, went to max pressure, then back to ambient with a hold time of 10 min at each interval. K-type thermocouples monitored the upstream and downstream temperature, and a flow controller measured the exhaust flow rate.

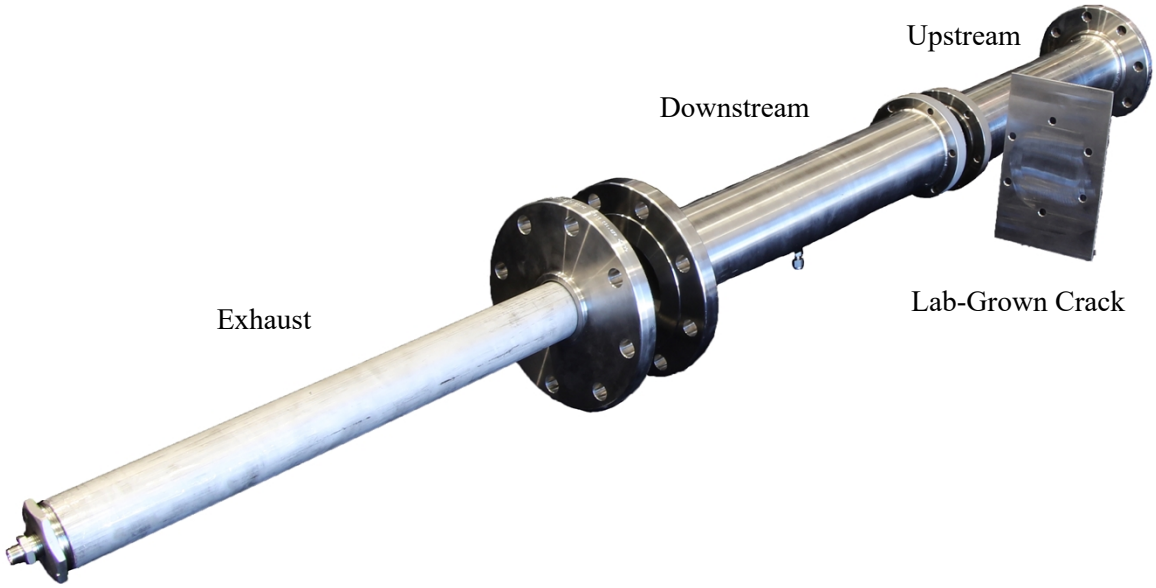

Figure 2.3 New test section for lab-grown crack testing.

2.2 Design of the Microchannel

The microchannel used in this study has a slot opening that gradually increases in a linear fashion from 13 µm to 25 µm, with the 13 µm depth facing the upstream portion of the test section as illustrated in Figure 2.4. The microchannel was fabricated from paired high-precision Mitutoyo gage blocks as shown in a schematic in Figure 2.5. The microchannel was formed by machining into the surface of one of the gage blocks using electrical discharge machining (EDM). The mounting holes were also cut using wire EDM. The paired halves of the gage blocks were bolted together to form the microchannel held in a mounting assembly as detailed in Figure 2.6. An isometric view of the microchannel mounted to the flow flange is shown in Figure 2.7.

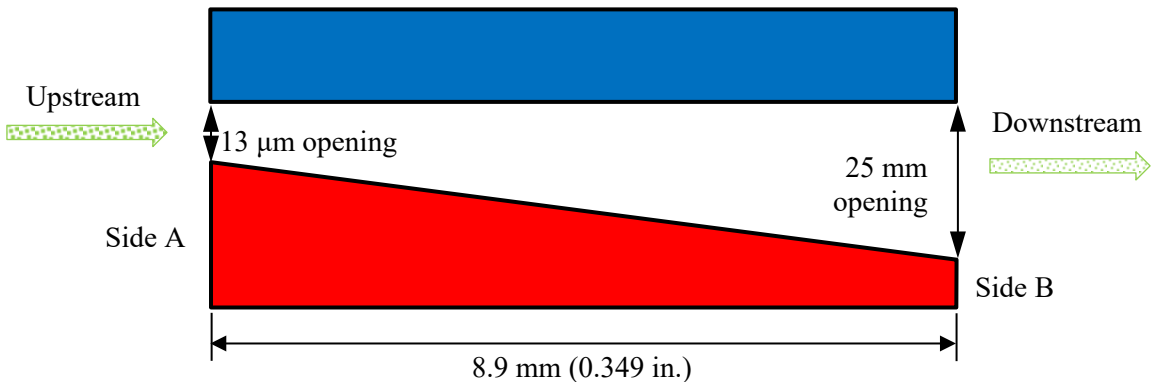

Figure 2.4 Illustration of the linear slot microchannel (not to scale).

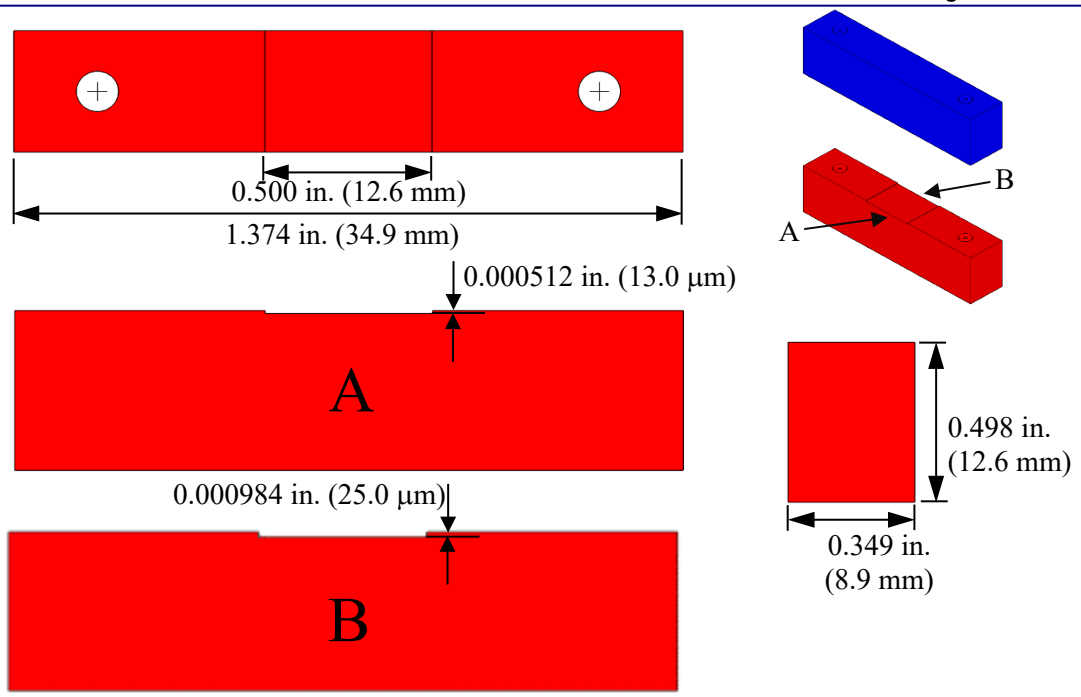

Figure 2.5 Schematic of the linear block (13 to 25 µm depth transition) microchannel assembly. Side A (13 µm depth) faces towards the upstream portion of the test section. Side B (25 µm depth) faces towards the downstream portion.

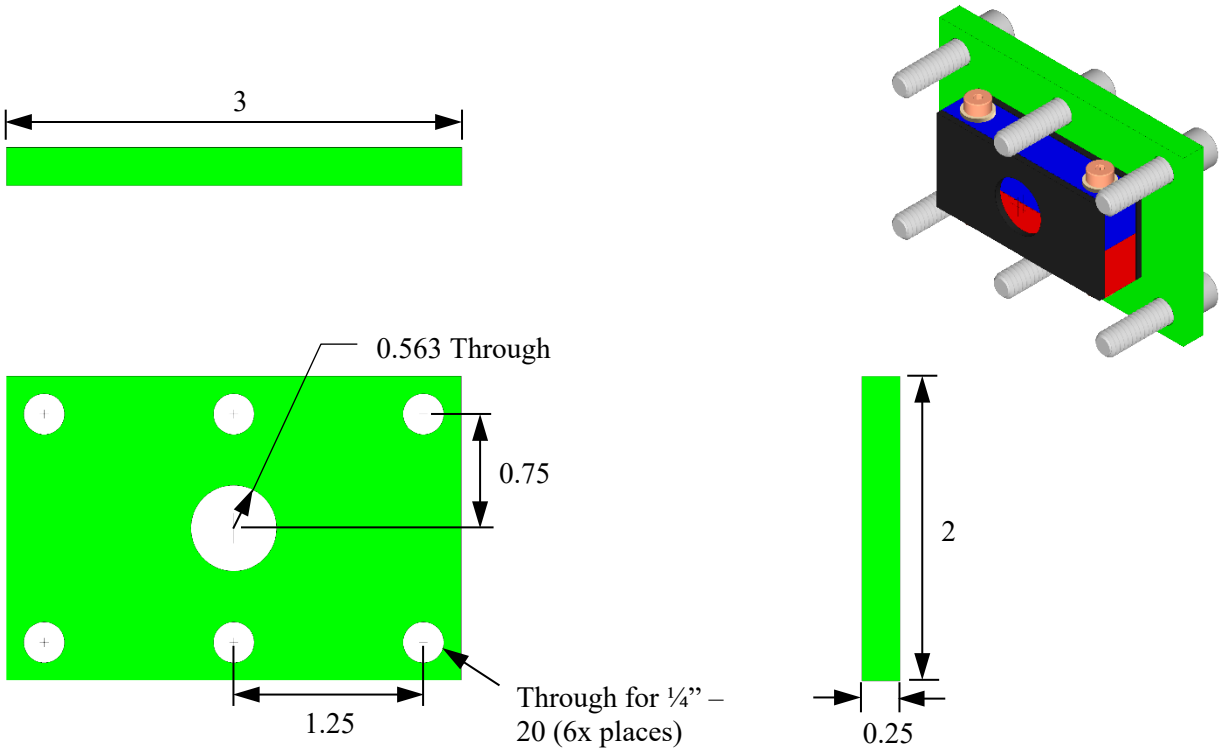

Figure 2.6 Details of the microchannel mounting assembly. All dimensions in inches.

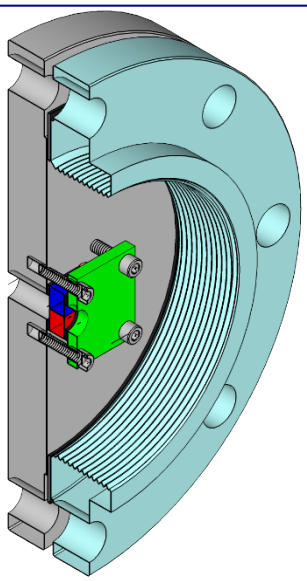

Figure 2.7 Isometric cutaway showing the microchannel mounted to the flow flange.

Figure 2.8(*a)* and Figure 2.8(*b)* show a profilometry image and a corresponding line scan of the linear microchannel block, respectively. These profiles were taken with a Keyence VK-X100 laser scanning microscope.

(a)

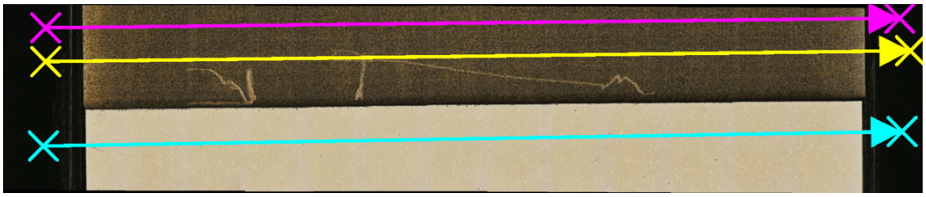

(b)

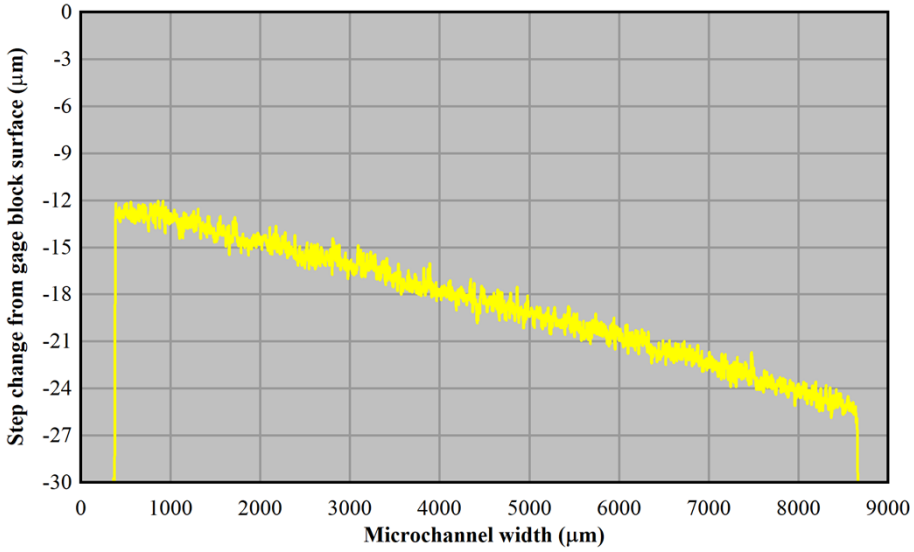

Figure 2.8 Profilometry image (a) and line scan of the linear block (13 to 25 µm depth transition) microchannel (b) using the Keyence laser scanning microscope.

The drop-offs in Figure 2.8(*b*) can be explained by the geometry of the microchannel block, which has chamfers along the edges of the block. Figure 2.9 shows these chamfers in more detail. The linear slope region spans 8.26 mm across the microchannel width, but the total width of the block is 8.89 mm, so 0.63 mm of the flow length is chamfered.

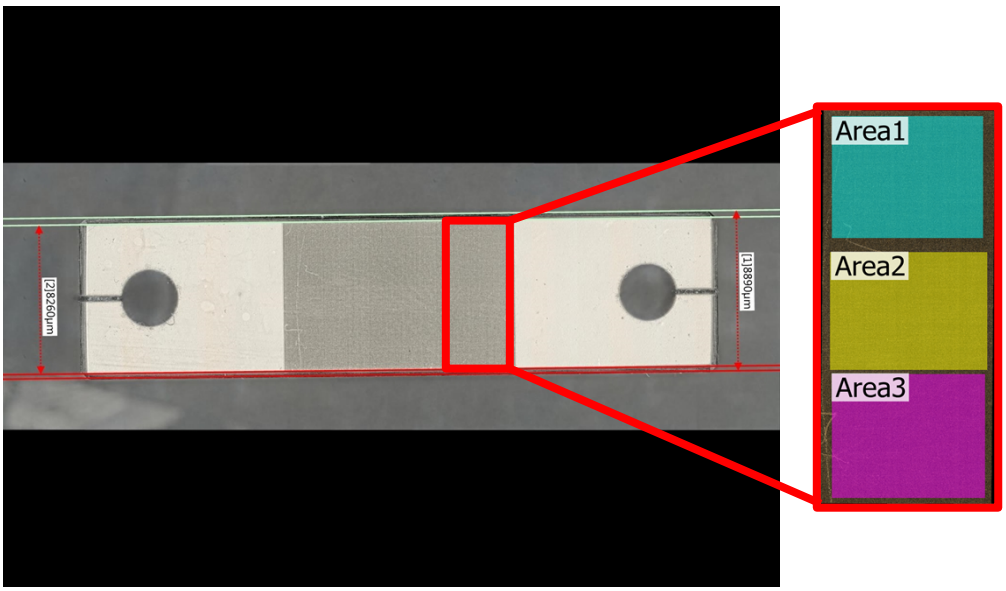

Figure 2.9 Optical microscope image of the linear block detailing the chamfered regions, and the region used to characterize the surface roughness.

The surface roughness of the microchannel was also characterized with the Keyence VK-X100 laser scanning microscope by taking the arithmetical mean height (S_a) of three surface areas in a sub-region of the microchannel shown in Figure 2.9. The average S_a of the three areas was found to be 0.734 µm, which was on the same order of magnitude as the measured S_a values of the slot orifice microchannel used in previous testing (0.408 and 0.386 µm for the left and right sides of the microchannel region, respectively) [Durbin *et al*., 2020].

2.3 EPRI Lab-Grown Crack Description

Two lab-grown crack samples were provided to SNL by EPRI and are referred to as LT-14 and LT-28. The plates were initially created for mitigation and repair testing and were created by placing the ½-inch 304 H SS plates in a 3-point bending apparatus while exposing one side to an aggressive salt solution [EPRI, 2022]. 3-point bending resulted in tensile stresses in half the thickness of the sample and compressive stresses in the other half. The crack propagated to the midplane of the plate, and wire EDM was used to remove the uncracked thickness of the plate resulting in a sample with a through wall SCC less than half the thickness of the original plate. The final plate thickness after planning to flush and polishing was approximately 5.65 mm. Figure 2.10, Figure 2.11, Figure 2.12, and Figure 2.13 show sample LT-14 side 1 (LT-14S1), LT-14 side 2 (LT-14S2), LT-28 side 1 (LT-28S1), and LT-28 side 2 (LT-28S2) respectively. In both samples side 2 was the side exposed to the salt solution, was under the greatest amount of tensile stress from the 3-point bending apparatus, and results in a greater crack opening displacement compared to side 1.

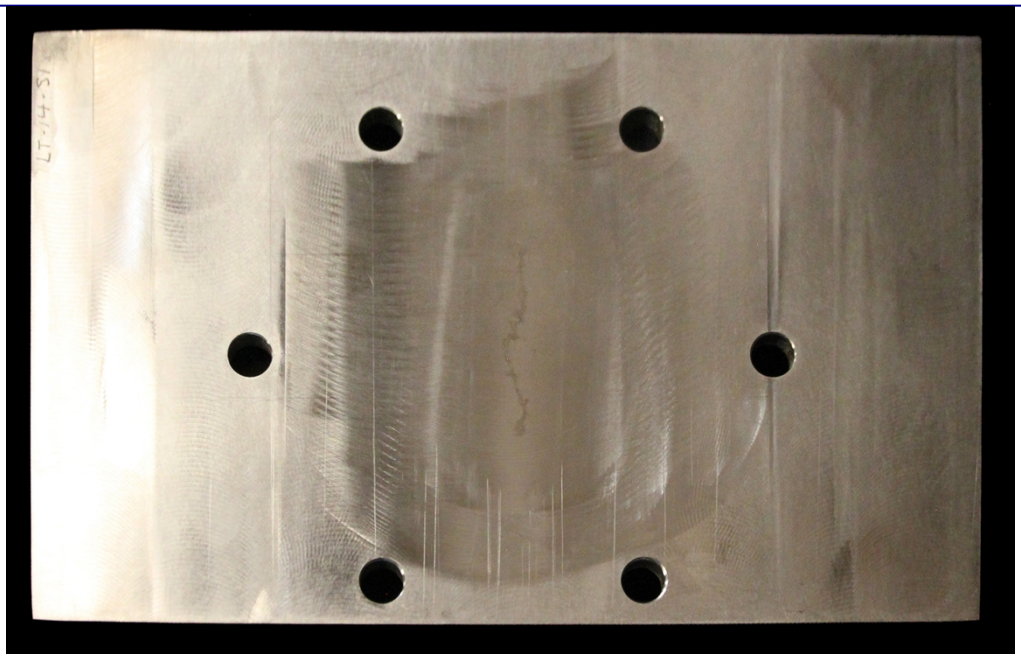

Figure 2.10 EPRI crack sample LT-14S1.

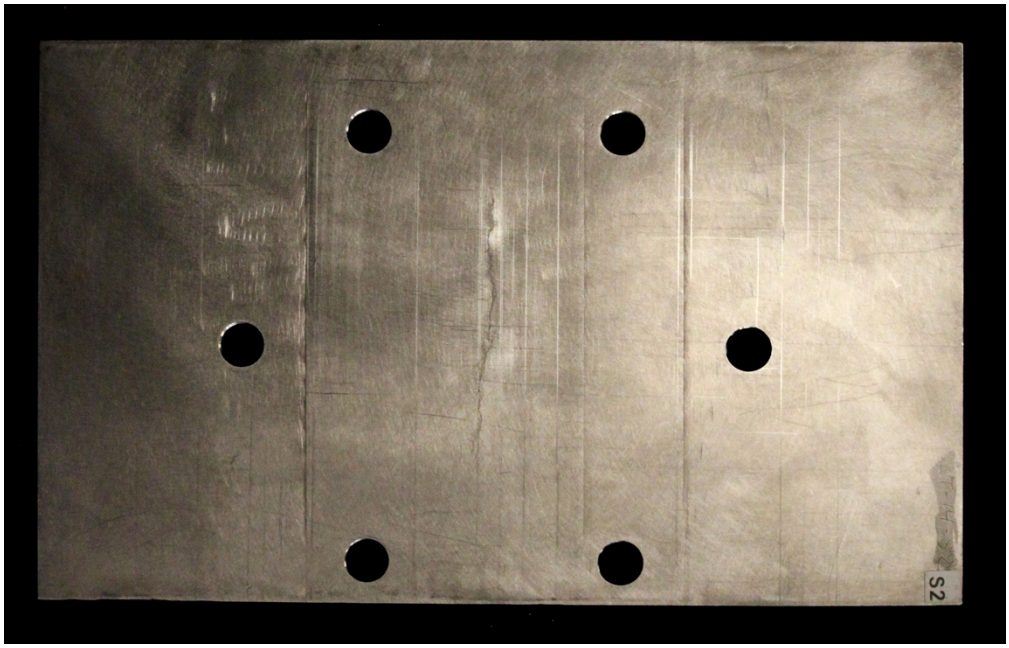

Figure 2.11 EPRI crack sample LT-14S2.

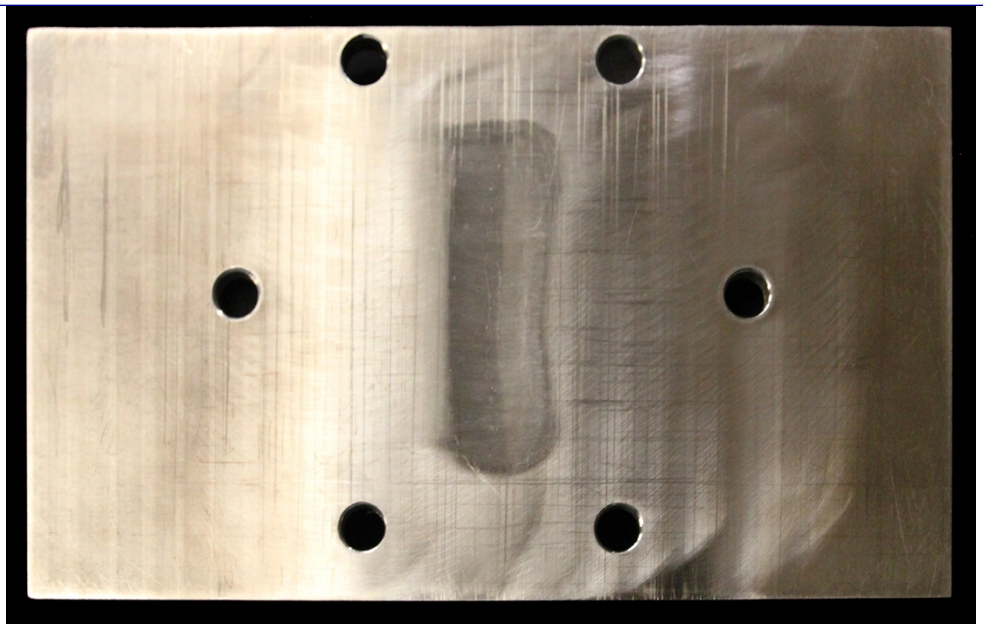

Figure 2.12 EPRI crack sample LT-28S1

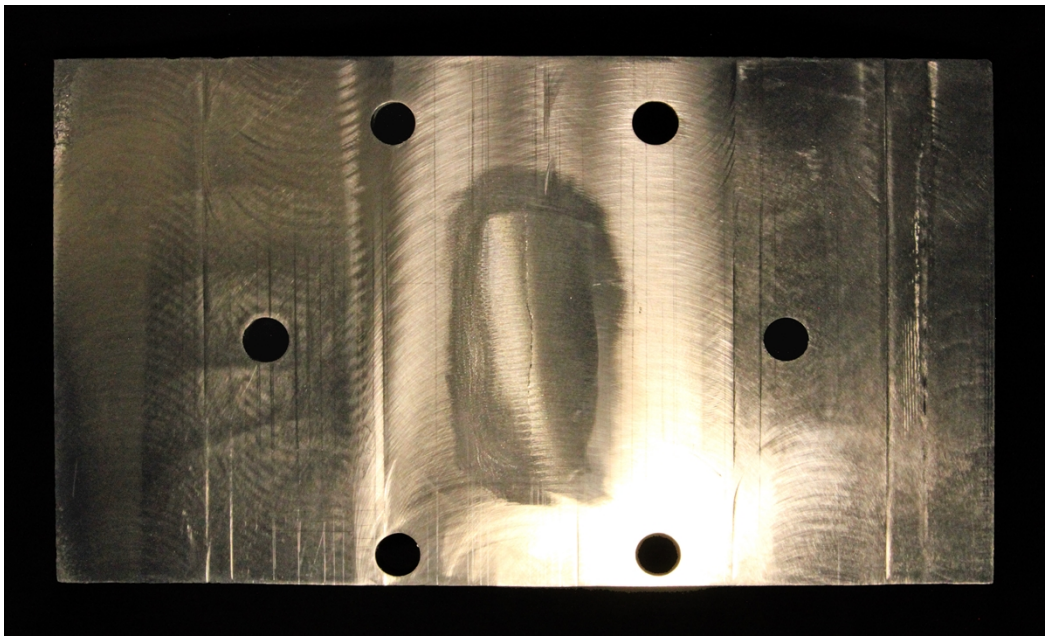

Figure 2.13 EPRI crack sample LT-28S2

Prior to flow testing, the cracks were characterized using non-destructive optical techniques to determine basic geometrical parameters such as crack length and crack opening displacement [J. Faubel, 2023]. The cracks were imaged with a Keyence laser scanning confocal microscope and topographical maps of the plate surfaces were subsequently generated. Shown in Figure 2.14 is a small portion of topographical map of LT-14S1. Blue represents areas of higher elevation and red represents lower. Locations of increased depth compared to local plate elevation were said to belong to the crack feature and the physical dimension of the pixels were used to quantify the size of said features.

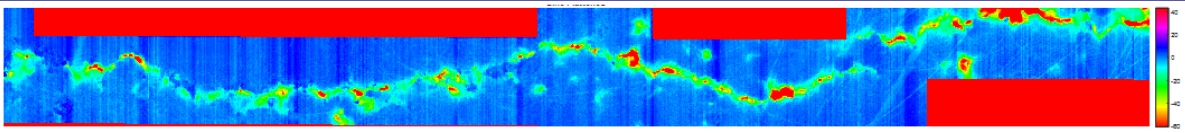

Figure 2.14 Topographical map of a portion of the surface of LT-14S1.

A threshold value for local elevation was chosen through best judgement and a binary mask of the crack was generated. The masks of both crack samples are shown in Figure 2.15. Each white pixel is said to belong to the crack, and by summing up the number of white pixels in each column along the long axis of the figure in conjunction with the physical dimension of the pixel, the crack opening displacement was evaluated. The crack opening displacement as well as total crack length are shown in Table 2.1. It should be noted that in the case of LT-28 there is an additional smaller crack feature a few inches away from and not connected to the main crack feature, but it is unclear whether this crack propagates through the entire thickness of the sample.

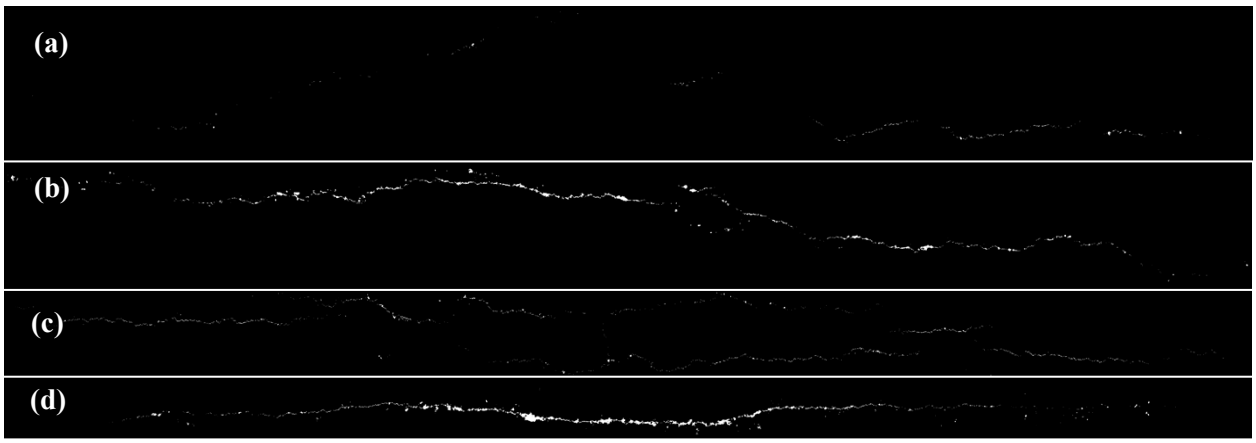

Figure 2.15 Masks generated for the EPRI crack samples LT-14S1 (a), LT-14S2 (b), LT-28S1 (c), and LT-28S2 (d).

Table 2.1 Crack opening and length for EPRI sample LT-14 and LT-28.

	LT-14		LT-28	
	Side 1	**Side 2**	**Side 1**	**Side 2**
Crack Opening Displacement (μm)	8.27	67.70	10.31	14.99
Total Crack Length (mm)	47.25	69.44	71.95	74.88

The final notable difference between the two crack samples is the bifurcated nature of the crack in sample LT-28. A zoomed in view of LT-28S1 is shown in Figure 2.16 (*a*). Figure 2.16 (*b*) shows an SEM image with extents as the red box in part (*a*). Figure 2.16 (*c*) is a 3D Computational Tomography Scan (CT-scan) of the crack in sample LT-28. Two parallel cracks are plainly visible in the zoomed in image, and the SEM image shows there are minimal features connecting the two. The CT-scan only affords a qualitative evaluation of the crack because the physical dimensions of the plate negatively impacted the resolution of the acquired image, but it does appear that both parallel crack features converge towards the middle of the figure and communicate with the single feature of side 2.

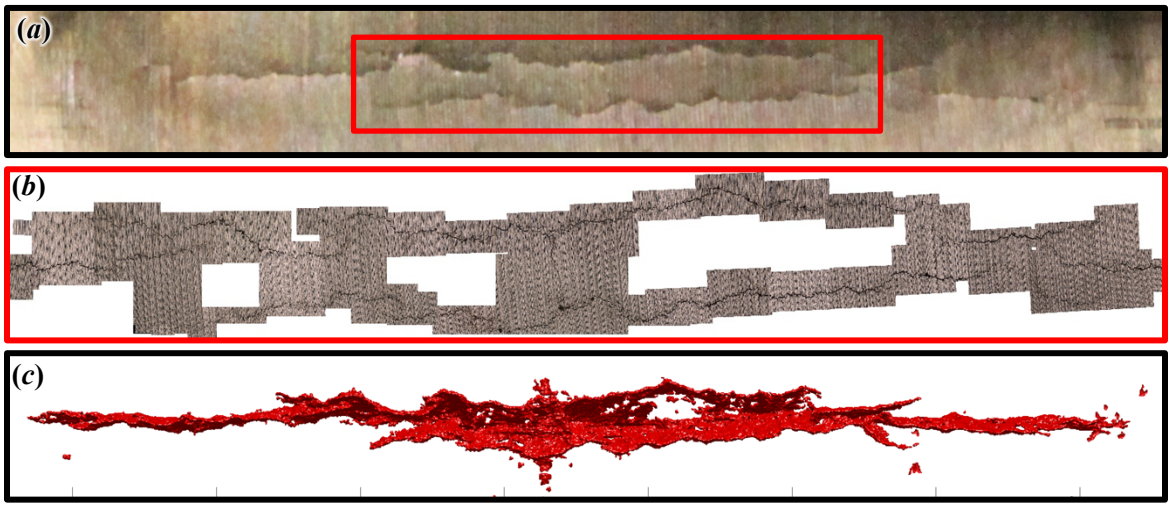

Figure 2.16 (*a*) Zoomed in optical image of LT-28S1, SEM image of crack (*b*), and (*c*) three-dimensional CT-Scan of LT-28 looking from the same plane as (*a*). The extent of image (*b*) indicated by red box in (*a*).

2.4 Instrumentation

The following instrumentation was used to characterize these tests. All stated uncertainties are assumed to represent 95% confidence intervals unless otherwise stated.

2.4.1 Pressure

The pressure in the aerosol storage tank was monitored with a 1,034 kPa (150.0 psia) Setra Model ASM transducer. Pressures on the upstream and downstream sides of the test section were monitored using a 1,034 kPa (150.0 psia) and a 103 kPa (15.0 psia) Setra Model ASM transducer, respectively.

The uncertainty of all the Setra pressure transducers is < ± 0.05% full scale (FS).

Table 2.2 Summary of pressure transducers.

Location	Model No.	Full Scale (kPa)	Uncertainty (kPa)
Storage tank	ASM1-150P-A-1M-2C-03-A-01	2,068	1.03
Upstream	ASM1-150P-A-1M-2C-03-A-01	1,034	0.52
Downstream	ASM1-015P-A-1M-2C-03-A-01	103	0.05

2.4.2 Temperature

All temperature measurements were taken with K-type thermocouples with standard calibration. The suggested, combined uncertainty in these measurements including data acquisition, cabling, and positioning errors is 1% of the reading in Kelvin [Nakos, 2004].

2.4.3 Mass Flow Rate

Flow from the test section was measured by a low pressure drop mass flow meter (Alicat, MW-20SLPM for upstream nominal pressures of 350 kPa, 500 kPa, 650 kPa, and 800 kPa; MW-2SLPM for an upstream pressure of 200 kPa). The standard liter per minute (slpm) is defined as one liter of air flow at standard temperature and pressure (STP) (*i.e.,* reference density of $\rho_{STP} = 1.184$ kg/m^3). The mass flow meters used during testing are presented in Table 2.3 and were chosen based on the best match between the starting mass flow rate of each test and the full scale of the mass flow meter. All Alicat flow meters and

controllers used are configurable for different gasses, and the presets for air or helium were selected depending on test.

For all the mass flow meters and controllers, the reported 95% uncertainty is ± (0.4% of reading + 0.2% FS) for a maximum of ± 0.6% FS.

Table 2.3 Summary of mass flow instrumentation.

Description	Model No.	Full Scale Q_{STP} (slpm)	Uncertainty (slpm)
High flow downstream exhaust	MW-20SLPM	20	0.12
Mid flow downstream exhaust	MW-10SLPM	10	0.060
Low flow downstream exhaust	MW-2SLPM	2	0.012
High pressure aerosol sensor	MC-5SLPM	5	0.030
Low pressure aerosol sensor	MC-5SLPM	5	0.030

2.4.4 Aerosol Spectrometer and Aerosol Sensors

The Palas Promo 3000 HP is a flexible, light-scattering aerosol spectrometer system that uses twin optical sensors to determine quasi-simultaneous particle concentration and particle size at two locations. Fiber-optic cables (light wave conductor or LWC) are used to carry light from the main controller to the remote Welas 2200 high pressure aerosol sensors as well as the resulting light-scattering signal from the remote sensors back to the main controller. The Welas 2200 sensors are specially designed to require only 0.5 alpm of flow through the sampling chamber. This high-pressure aerosol sensor is capable of directly measuring samples at pressures up to 1,000 kPa. Rapid fiber optic switching allows a single instrument to analyze the upstream and downstream aerosol sensors in quasi-simultaneous fashion. A single Promo 3000 HP and Welas 2200 sensor was used to continuously monitor aerosol in the tank.

In sensor switching mode, the instrument collected data from the upstream sensor for 55 seconds, required 5 seconds to switch to the downstream sensor, then collected data from the downstream sensor for 55 seconds. Data was collected at a sample frequency of 1 hz except for the 5 second interval required for sensor switching.

The aerosol spectrometer characteristics are summarized in **Error! Reference source not found.**. The spectrometer can measure concentrations up to 10^6 particles/cm^3 depending upon the model of the Welas sensor. The spectrometer is ideally suited to simultaneously monitor the aerosols from the high-pressure upstream and low-pressure downstream side of the simulated crack for aerosol size and concentration characteristics. The Welas 2200 can make reliable measurements over a concentration range from 1 to 1.6 × 10^4 particles/cm^3. The Promo spectrometer will still analyze concentrations in excess of the Welas sensor limit, but it will introduce coincidence error defined as an undercounting of the number of particles and an over estimate of the particle diameter particles because too many particles occupy the measurement volume simultaneously.

Table 2.4 Summary of the aerosol spectrometer capabilities.

Instrument Characteristic	Value
Aerosol size range	0.3 to 17 µm
Aerosol size channels	64/decade
Minimum Particle Concentration	1 particle/cm^3
Maximum Particle Concentration	1.6×10^4 particles/cm^3
Maximum Sample Pressure	1,000 kPa
Maximum Sample Temperature	120 °C

Calibration of the Promo is conducted using a monodisperse aerosol of known particle diameter. During calibration, the Promo determines the length of the light-scattered signal (pulse width) which is the time of flight (converted to velocity) of a particle through the measurement volume. The user then inputs the measured particle velocity, and the Promo uses the user specified value to correctly map the signal to the appropriate spectrometer channel. Actual particle velocity that deviates from the user specified velocity value will introduce error into the reported concentration and cause the Promo to mis-categorize particles into the wrong size bin.

It was previously thought that the use of flow controllers to maintain sample flow at a constant volumetric flow rate of 0.5 alpm would ensure that the flow velocity through the detection volume remained constant over all operating pressures. This was not the case, and the discrepancy was due to the customized "low-flow" Welas sensors. The standard Welas sensor configuration operates at a volumetric flow rate of 5.0 alpm, which was not suitable for this testing. Regardless of sensor configuration, the Promo requires a consistent particle velocity, i.e. time of flight, through the detection volume. In order to maintain consistent particle time of flight for the 0.5 alpm configuration, Palas uses a flow restriction nozzle to accelerate the particles through the detection volume. It is understood that this nozzle introduces the pressure and carrier gas dependence.

To account for pressure dependence, an additional calibration step was introduced in FY22. Calibration prior to the test with the monodisperse aerosol remains unchanged. Once the tank is seeded and at operating pressure, the two-inch ball valve is briefly opened to allow some particles into the upstream test section. The Promo measures the cerium oxide (CeO_2) particle velocity, and that value is input as the new user specified velocity.

2.4.5 Aerosol Generator

The aerosols were actively seeded into the pressure tank with a Palas RBG Professional (Figure 2.17(*a*)). The RBG Professional can deliver particles at a rate between 38 mg/h to 800 g/h. The heart of the instrument is the rotating brush (Figure 2.17(*b*)). The desired aerosols to be dispersed are packed into a cylinder. A transport piston slowly pushes the bed of packed powder into the rotating metal bristle brush that dislodges particles and holds them in the bristles. When the brush rotates 180 degrees further, the bristles are exposed to a flow of dispersion carrier gas that suspends the particles and transports them away, creating a polydisperse distribution of desired aerosol. The RBG has a maximum operating pressure of 1000 kPa which is greater than the maximum operating pressure of 200 kPa for the RBG 1000 used in previous testing. The higher operating pressure of the new unit allows for active seeding throughout the duration of a test.

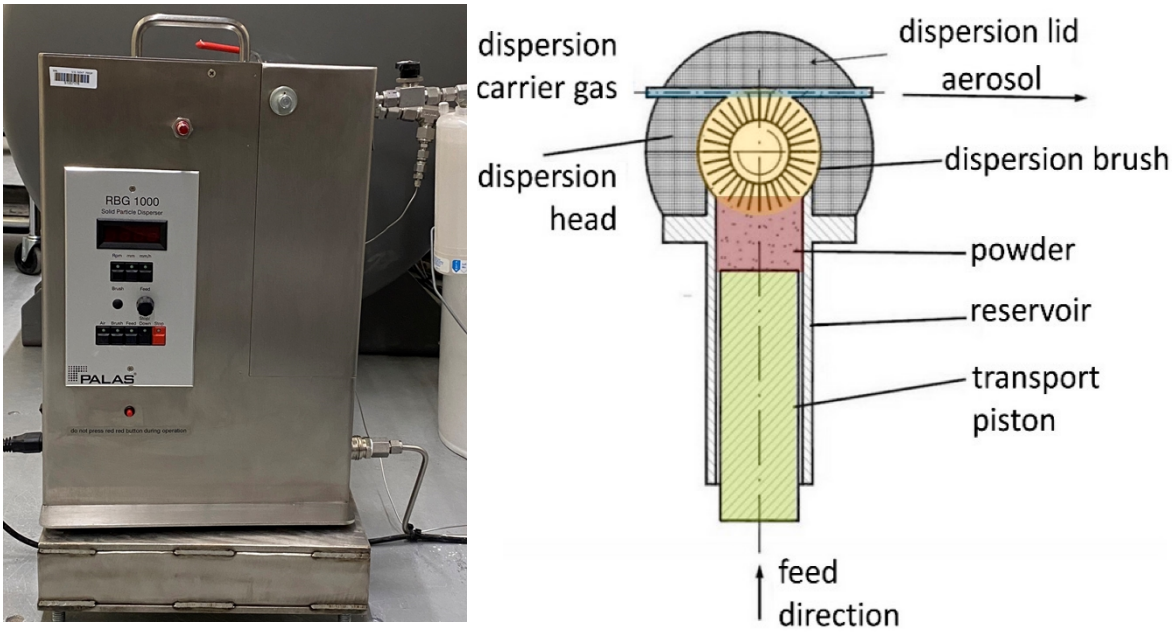

(*a*) (*b*)

Figure 2.17 Image of the Palas RBG Professional (*a*) and diagram of the rotating brush (*b*). [Palas GmbH, 2002]

2.5 Aerosol Characteristics

2.5.1 Selection of Surrogates

Cerium oxide was chosen as the surrogate for spent nuclear fuel ($\rho_{SNF} \approx 10$ g/cm^3) because of its relatively high density ($\rho_{CeO2} = 7.22$ g/cm^3) and its commercial availability. For CeO_2, an AED particle size of 10 µm equates to a geometric particle size of 3.72 µm. Geometric particle size is used exclusively through the remainder of this report. Figure 2.18 shows the particulate sizes as characterized by the probability distribution function (PDF) and cumulative distribution function (CDF) of the surrogate used in these tests. Here, the distributions are plotted as a function of geometric diameter (bottom) and AED (top). This specific lot of CeO_2 was chosen because the particulates were concentrated in the respirable range (AED < 10 µm). The mass median diameter (MMD) was 2.4 µm, the geometric standard deviation (GSD) was 1.9, and ~75% of the particles (by mass) were respirable (AED < 10 µm). Fifty percent of the measured particles have a mass smaller than the MMD (also known as D_{50}), and 50% of the measured particles have a mass that is greater.

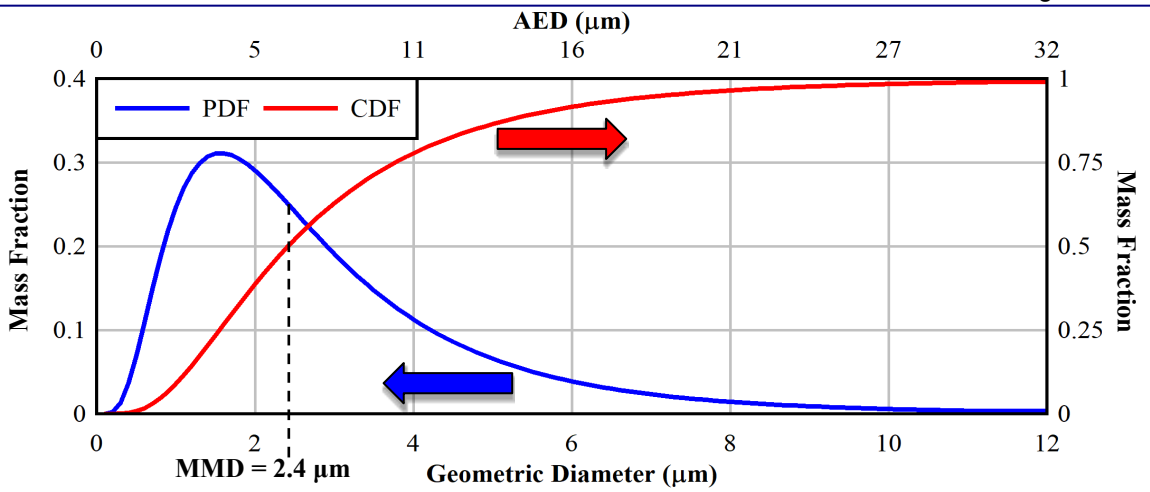

Figure 2.18 Size distributions of the cerium oxide surrogates used in testing.

2.5.2 Reference Initial Aerosol Concentration

The particulates released from SNF were characterized when air was forced through segmented fuel [Hanson *et al.*, 2008]. The geometric particle size data from nine tests conducted on four fuel rod segments are summarized in Figure 2.19. The average of the nine tests yielded an MMD of 3.46 µm (geometric diameter), a GSD of 2.24, a total release fraction of 1.9×10^{-5} of which 46% was respirable for a respirable release fraction of 8.9×10^{-6}. This respirable release fraction is in reasonable agreement with 4.8×10^{-6} cited in NUREG-2125 [NRC, 2012] and 3×10^{-6} cited in SAND90-2406 [Sanders, *et al.*, 1992].

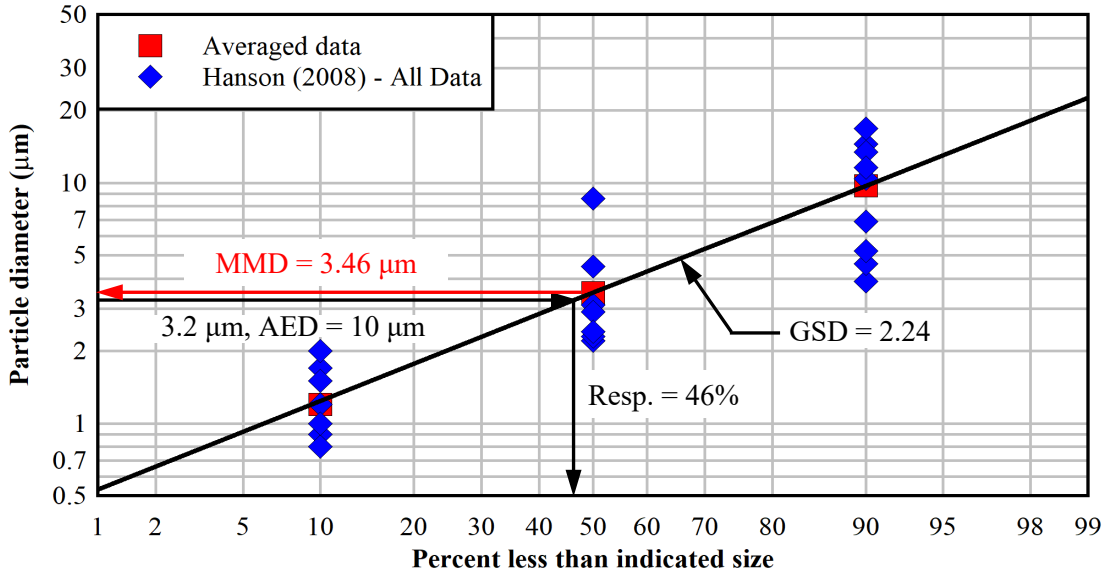

Figure 2.19 Respirable fraction of spent fuel from Hanson *et al.*, 2008.

To estimate an upper aerosol density for spent fuel dry storage, a canister with 37 pressurized water reactor (PWR) assemblies with a uranium oxide (UO_2) fuel mass of 520 kg per assembly was assumed. One percent of the fuel was assumed to fail simultaneously due to an undefined event. The canister was assumed to have an internal free volume of 6 m^3 and a starting initial pressure of 800 kPa (116 psia). The equivalent aerosol density for this assumed system at STP is approximately $C_{m,\,STP} = 54$ mg/m^3. The maximum particle concentration without coincidence error was between 5 and 10 mg/m^3 at STP

depending on operating pressure. For all testing described in this report, the standard temperature and pressure were taken as the default values for the mass flow rate instruments (Alicat MC and MW Series) of 298.15 K (25 °C) and 101.353 kPa (14.7 psia).

This page is intentionally left blank.

3 RESULTS

3.1 Clean Flow Tests

3.1.1 Micro-Channel

The mass flow rate characteristics of the engineered microchannel used in this study were first evaluated in the absence of aerosols. All clean flow tests were conducted with the Promo aerosol sensors off, to allow all gas to exhaust through the microchannel and exhaust pathway. Clean flow refers to testing without the introduction of the surrogate particulates, as opposed to the aerosol-laden tests. The flow results with air and helium are summarized in Figure 3.1, which shows the air mass flow rate through the clean microchannel as a function of a wide range of pressure drops. Also shown for reference are the initial pressure drops considered in the aerosol-laden tests: nominally 120 kPa, 270 kPa, 420 kPa, 570 kPa, and 720 kPa, indicated in Figure 3.1 by solid black circles. The velocity through the microchannel is roughly the same for both gases at the same pressure differential, but the mass flow rates are significantly different because the density of air is greater than helium by a factor of roughly 7.2 for a given pressure. The average ratio of the measured mass flow of clean air and helium was 7.3 over the range of pressure differential values in Figure 3.1.

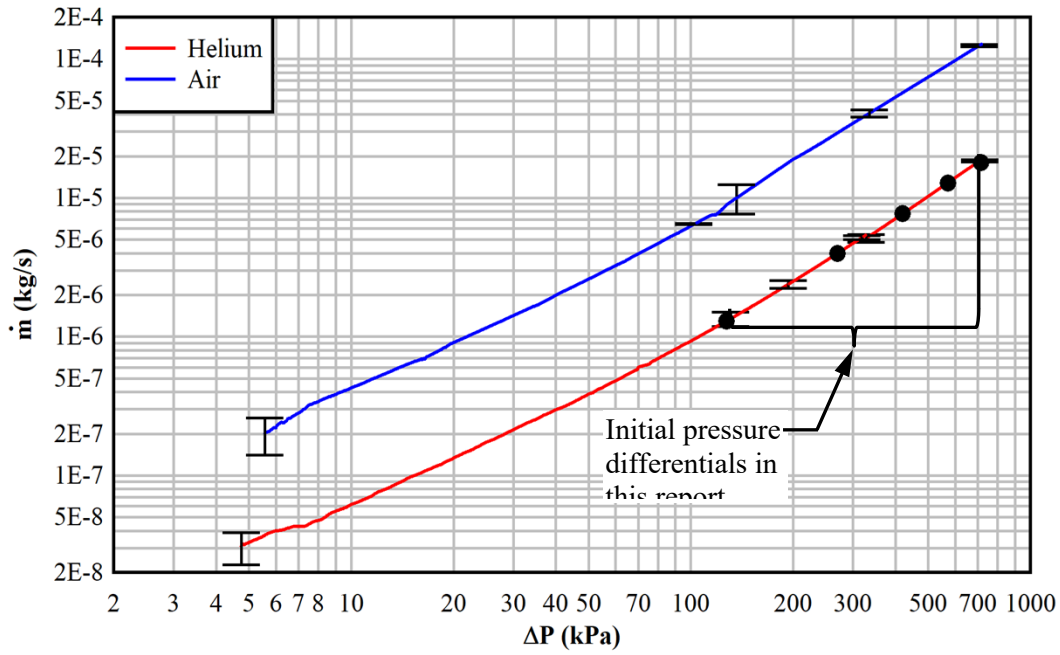

Figure 3.1 Mass flow rate as a function of pressure drop across the linear microchannel for air (blue line) and helium (red line).

3.1.2 EPRI Lab-Grown Cracks

The mass flow rate characteristics of the EPRI lab-grown cracks were also evaluated in the absence of aerosols. Because the lab-grown crack clean flow tests were conducted in the tank bypass test section described in Section 2.1, the results are presented as discrete data points at each upstream dwell pressure. The results for EPRI crack sample LT-14 are presented in Figure 3.2 along with the microchannel clean flow blowdown results for comparison. Using the reported dimensions of LT-14 shown in Table 2.1 and approximating the crack as an ellipsoid, the upstream flow area is 0.307 mm^2 and the downstream flow area is 3.692 mm^2. The microchannel has an upstream flow area of 0.164 mm^2 and a downstream flow

area of 0.340 mm^2. The larger upstream and downstream flow areas for crack LT-14 is less restrictive than the microchannel and is reflected in the measured flow rate accordingly.

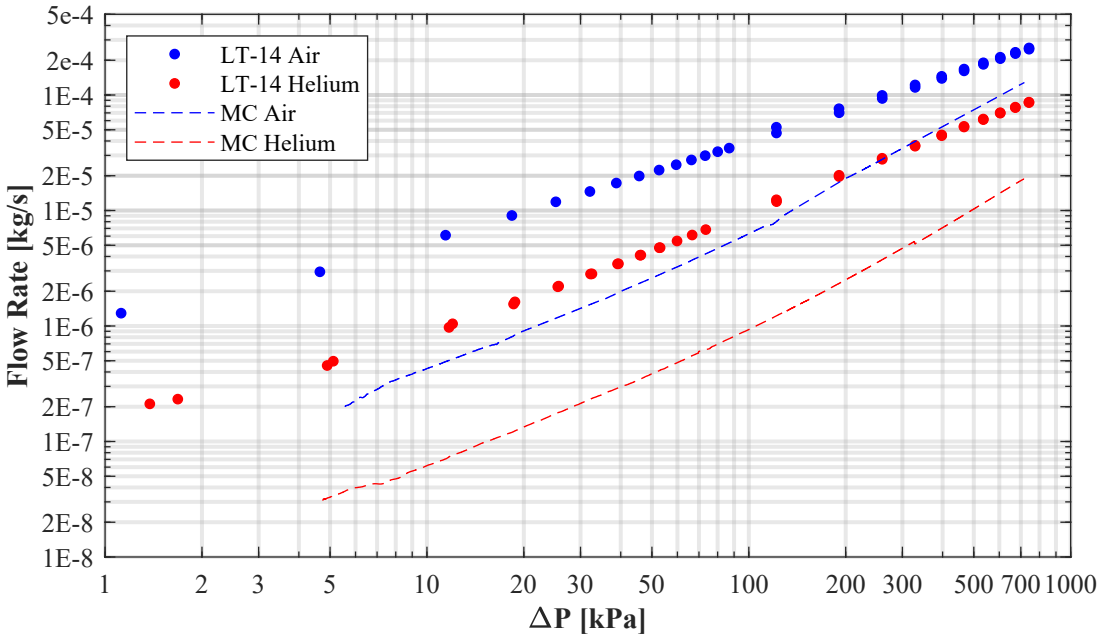

Figure 3.2 EPRI sample LT-14 mass flow rate as a function of pressure drop for dry air and helium along with the microchannel flow for comparison.

The results for EPRI crack sample LT-28 are presented in Figure 3.3 along with the microchannel clean flow blowdown results for comparison. Sample LT-28 has a much smaller downstream crack opening compared to LT-14. The upstream approximate flow area is 0.583 mm^2 and the downstream flow area is 0.882 mm^2. These values are much closer to the microchannel flow areas and results in similar flow rates.

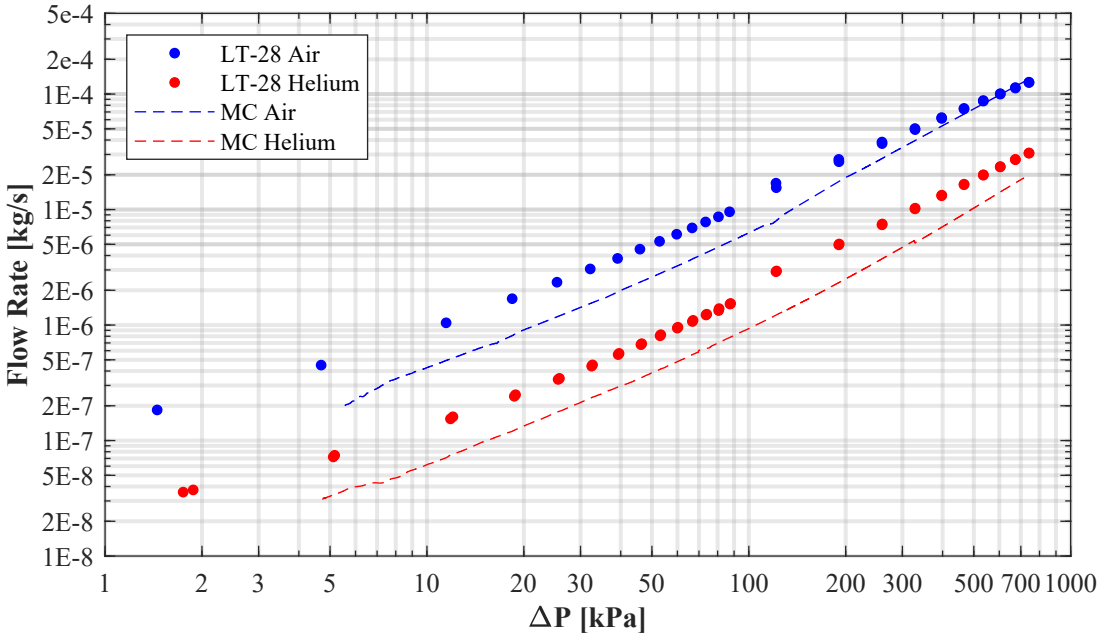

Figure 3.3 EPRI sample LT-28 mass flow rate as a function of pressure drop for dry air and helium along with the microchannel flow for comparison.

3.2 Aerosol-Laden Flow Tests

Summarized in Table 3.1 are the results for the aerosol testing through the microchannel with active seeding of aerosols into the tank with nominal upstream pressures of 350 kPa, 500 kPa, 650 kPa, and 800 kPa. One test was conducted with dry air, 800 kPa on 7/25/2023, and the rest were conducted with helium. Shown in Table 3.1 are the average particle concentration, mass concentration at SPT, MMD, and GSD over the integration period of the test. The final two columns are the integrated mass and transmission fractions. The methods for determining these values are defined in Section 3.2.1. Transmission fraction as a function of pressure drop across the microchannel is plotted in Figure 3.4

Table 3.1 Active seeding aerosol testing results.

Date	Nominal Pressure (kPa)	Location	Average Values				Mass (mg)	Transmission Fraction
			Cn (P/m^3)	$C_{m,STP}$ (mg/m^3)	MMD (µm)	GSD		
6/29/2023	350	Upstream	7193.60	21.04	2.49	1.67	14.02	0.0441
		Downstream	1175.25	0.92	1.05	2.27	0.62	
7/18/2023	350	Upstream	11381.33	18.26	2.14	1.75	15.78	0.0316
		Downstream	339.56	0.52	1.34	1.66	0.50	
7/5/2023	500	Upstream	14251.95	22.22	2.86	1.84	34.43	0.2084
		Downstream	3741.55	4.63	1.02	1.96	7.17	
7/12/2023	500	Upstream	13407.82	25.13	2.96	1.82	30.04	0.2074
		Downstream	3557.83	5.24	1.07	1.90	6.23	
7/20/2023	650	Upstream	11643.48	14.51	2.77	1.87	25.23	0.2931
		Downstream	3168.20	4.18	1.05	1.95	7.39	
7/21/2023	650	Upstream	12312.20	13.46	2.66	1.87	21.32	0.3308
		Downstream	2963.86	4.36	1.37	1.96	7.05	
7/25/2023	800	Upstream	11741.81	20.83	3.36	1.80	52.19	0.1544
		Downstream	2800.79	3.19	0.95	2.00	8.06	
7/25/2023*	800	Upstream	11053.75	11.09	3.17	1.99	37.92	0.2263
		Downstream	1872.67	2.51	1.23	2.29	8.58	

*Test on 7/25/2023 was conducted with dry air

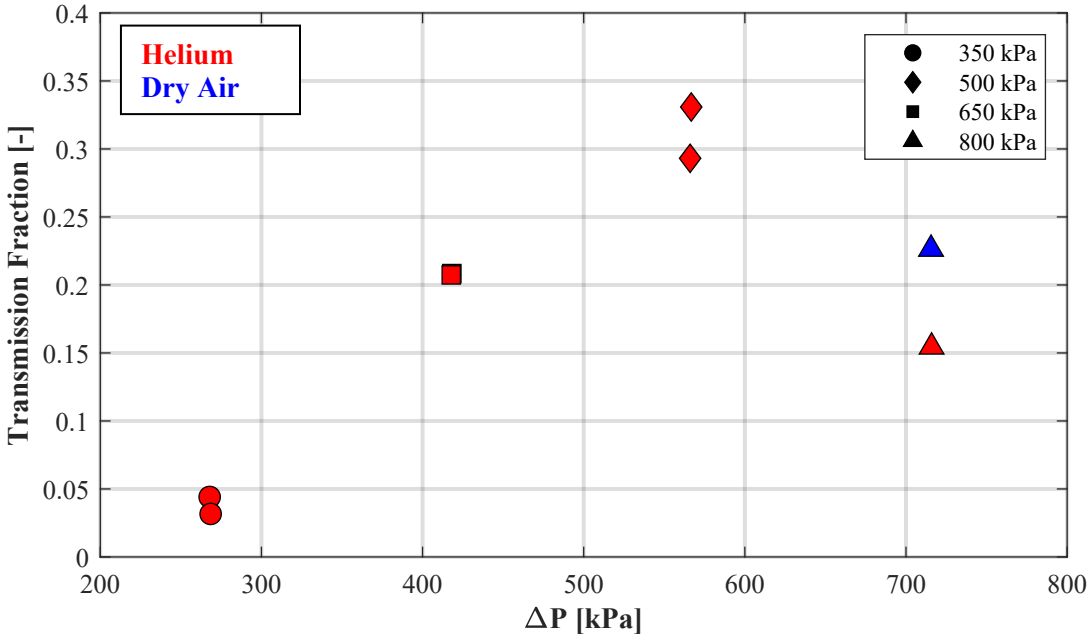

Figure 3.4 Integrated transmission as a function of pressure differential with active-seeding during the test.

3.2.1 Data Analysis

The measured instantaneous mass rate of aerosols upstream or downstream of the microchannel at any time *t* may be expressed as shown in Equation 3.1. Here, the mass flow rate of the background gas, Q_{STP} in units of m^3/s, at time *t* is multiplied by the mass concentration of aerosols, $C_{m,\,STP}$ in units of mg/m^3, at the same time *t*, both at STP conditions. The instantaneous transmission at time *t* is defined as the mass rate downstream divided by the corresponding instantaneous mass rate upstream as shown for the complementary instantaneous retention in Equation 3.2. The integrated mass transmitted to and from the microchannel is calculated as the integral of the instantaneous mass rate from a lower limit of t_o hours to an upper limit governed by the available aerosol data (τ) as shown in Equation 3.3. By taking the ratio of the downstream to the upstream integrated mass of aerosols, the integrated transmission of aerosols through the microchannel may be estimated (Equation 3.4). Because the mass flow of gas through the microchannel is conserved in the upstream and downstream calculation in Equation 3.1, the flow cancels in the calculation of the integrated transmission in Equation 3.4. Inherent assumptions are minimal aerosol wall and flow flange impaction losses between the upstream and downstream sample locations and quasi steady-state flow upstream and downstream of the microchannel.

$$m(t) = Q_{STP}(t) \cdot C_{m,STP}(t) \text{ [Units = mg/s]} \quad \textbf{3.1}$$

$$\text{Instantaneous Retention} = 1 - m_{Down}(t) / m_{Up}(t) \quad \textbf{3.2}$$

$$M(\tau) = \int_{t_o}^{\tau} m(t)\,dt \text{ [Units = mg]} \quad \textbf{3.3}$$

$$\text{Integrated Transmission} = M_{Down}(\tau) / M_{Up}(\tau) \quad \textbf{3.4}$$

3.2.1.1 Aerosol Concentration

Transmission of particulates through the microchannel was determined directly by measuring the aerosol concentration contemporaneously both upstream and downstream of the microchannel. In prior years testing, the raw temporal concentration data was fit to a fourth order log-log polynomial which was then integrated to evaluate the mass transmission. This technique worked well when the mass concentration exhibited well-behaved exponential decay due to particulate settling in the pressure tank. The data presented in this report were generated using an active seeding technique, and while every effort was made to establish constant upstream conditions, fluctuations were observed throughout the course of testing. To better accommodate these fluctuations, the upstream and downstream particulate mass transfer rates as defined in Eqn. 3.1 were fit with moving cubic splines prior to numerical integration.

Prior years analyses used 10 second collection intervals. Due to the fluctuation in particle size distribution from the active seeding, longer intervals were needed to provide a statistically significant representation of the aerosol population. Because the size distribution can vary significantly between 10 second intervals, the mass concentration would also vary in a similar fashion. To achieve a better statistical representation for each collection period, the collection interval was increased to 10 minutes. Each data point presented here is spaced apart by 10 minutes and is the sum of five-55 second intervals. Therefore, each data point shown in the analysis below represents a total collection time of 275 seconds.

Figure 3.5 shows an example of the upstream and downstream mass concentration transients for the helium test with active seeding conducted on July 5, 2023. The particle concentration data from the Promo 3000 HP was synchronized to the mass flow data collected by the DAQ by averaging the values in ±5 minutes intervals around the corresponding Promo data point. The averaged mass flow rate through the crack was used in Eq 3.1 with the corresponding Promo mass concentration to generate the upstream and downstream particle mass rates plotted in Figure 3.6. The red dashed lines represent the spline fits to the data and the vertical purple lines show the limits of integration used to evaluate the integrated mass and transmission fraction. The lower integration limit was chosen at the first data point to avoid the erroneous part of the spline fit which lacks physical meaning. The upper limit was chosen at the point at which active seeding terminated either due to loss of helium flow or exhaustion of the CeO_2 loaded into the RBG piston.

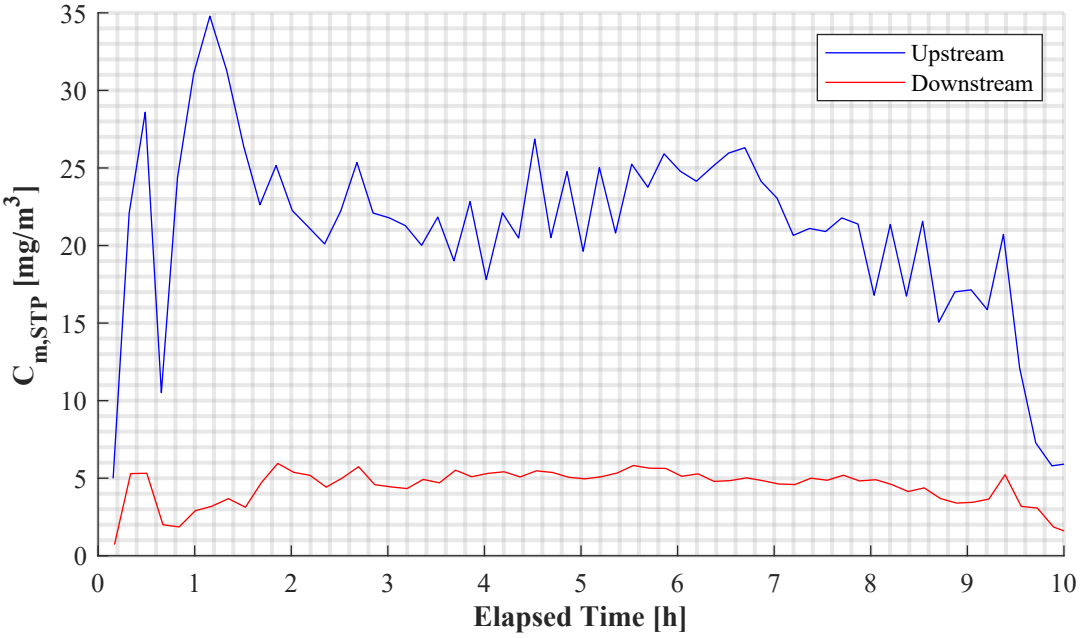

Figure 3.5 Raw aerosol mass concentrations for the helium test with active seeding conducted on 07/5/2023 with upstream pressure = 500 kPa.

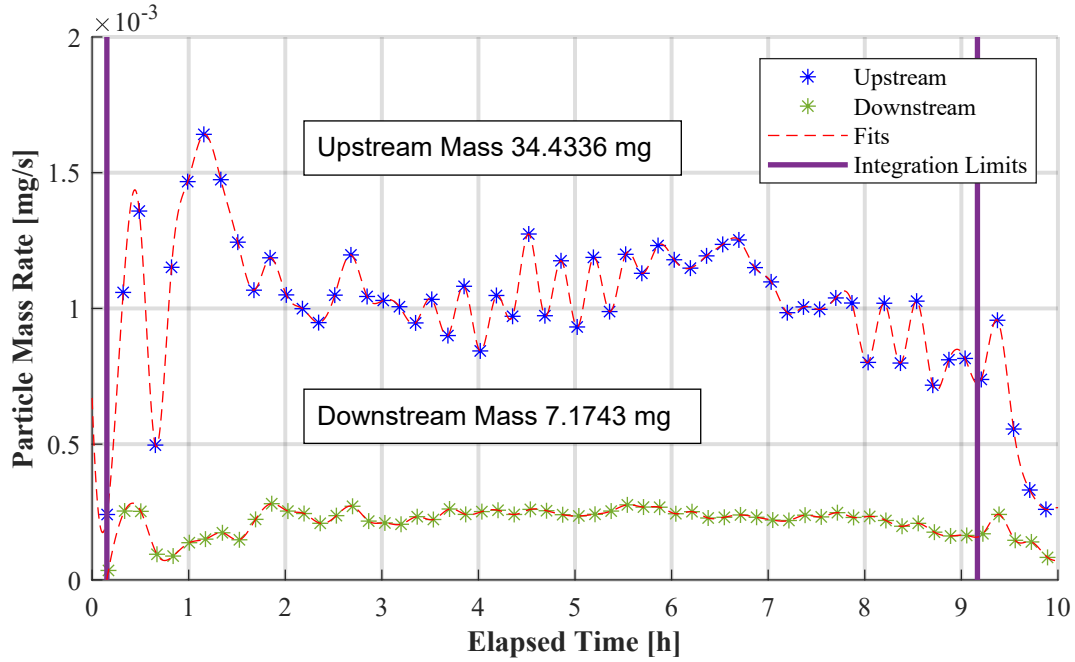

Figure 3.6 Particle mass rate with spline fits for integration for the helium test with active seeding conducted on 07/5/2023 with upstream pressure = 500 kPa.

Figure 3.7 shows a typical result of the integrated aerosol masses for the upstream and downstream sections on the left dependent axis for the test conducted on July 7, 2023. The ratio of the downstream to the upstream aerosol mass, *i.e.* integrated transmission, is shown on the right dependent axis. Fluctuations in the upstream mass concentration, shown clearly in the first 2 hours in Figure 3.6, propagates to the

integrated transmission fraction over that time period, but begin to average out to a fairly constant value as the test progresses, approximately 6 hours in this case. The upper integration limit for this test corresponds to when the helium supply was exhausted, and the upstream pressure began to decrease.

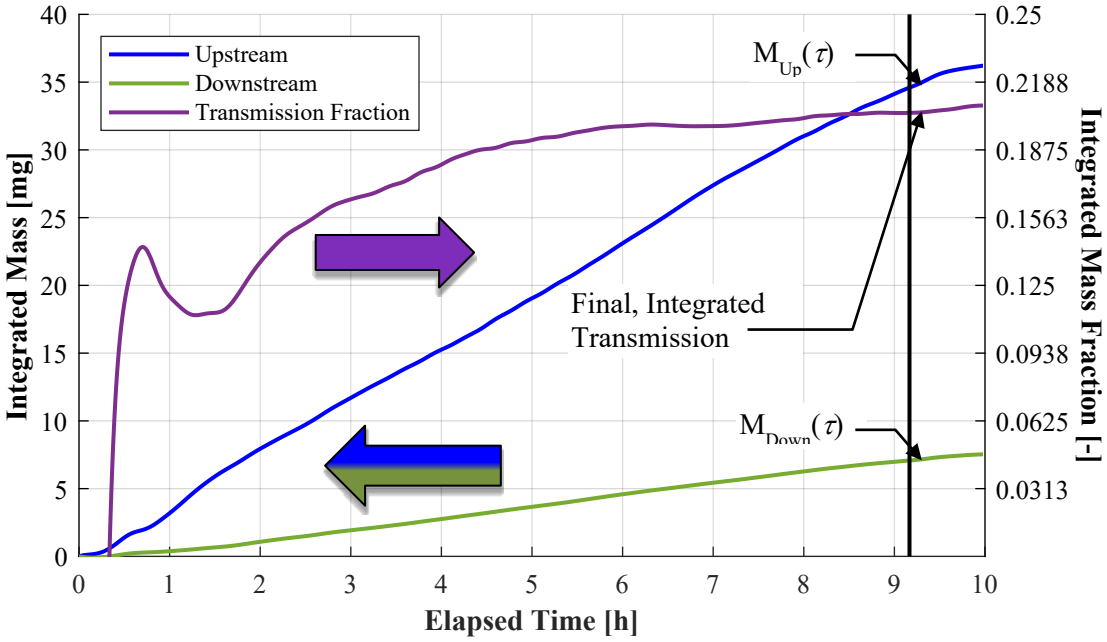

Figure 3.7 Integrated aerosol mass concentrations for the helium test with active seeding conducted on 07/5/2023 with upstream pressure = 500 kPa.

3.2.1.2 Aerosol Size Distribution

Figure 3.8 shows the particle distribution upstream and downstream of the crack throughout the course of the test conducted on July 5, 2023. The upstream fluctuations that occur on timescales < 1 hour are muted or nonexistent in the downstream transients. The black trendlines on the upstream and downstream 84th percentile series shows that over the course of a test, the behavior of the change in particle size distribution upstream is reflected in the downstream size distribution. Similar to the constant pressure testing of FY22, the difference between the upstream and downstream 84th percentile is greater than the 50th and 16th indicating that the crack is more effective at filtering larger particles than smaller ones. The transient upstream and downstream particle size distributions are recorded for each test.

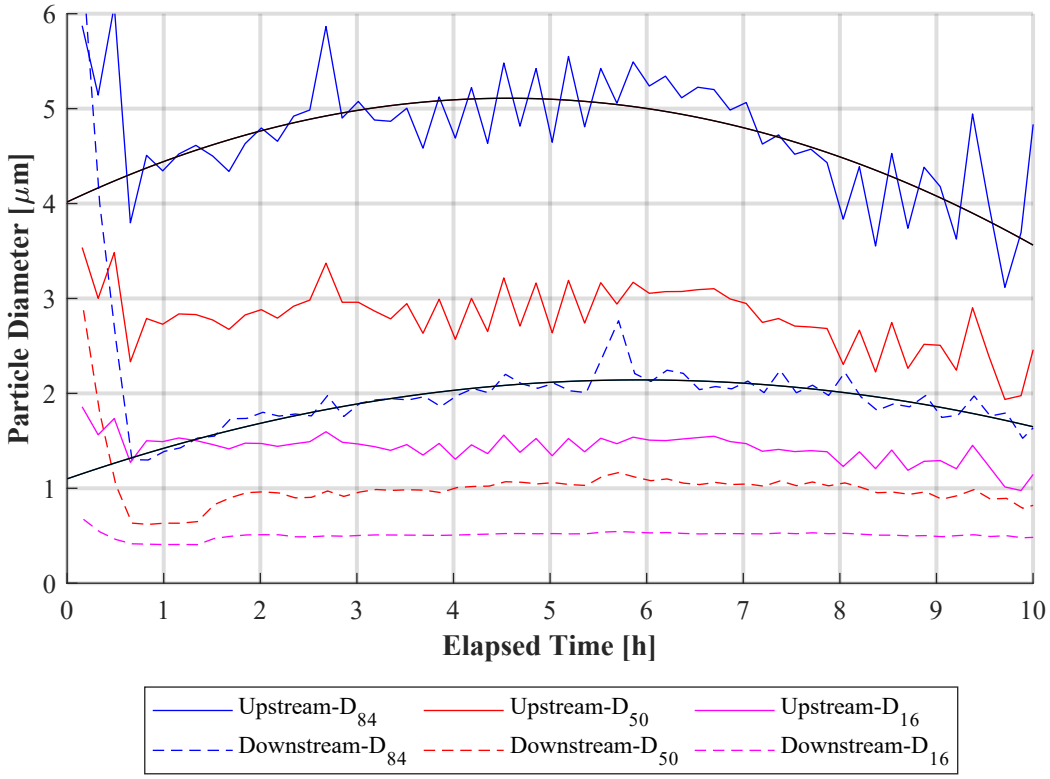

Figure 3.8 Particle diameter of the 84th, 50th, and 16th percentile by mass for the helium test with active seeding conducted on 07/5/2023 with upstream pressure = 500 kPa.

The MMD (shown as D_{50} in Figure 3.8) is the diameter at which 50% of the aerosol mass comprises of particles with diameters > D_{50}, and 50% of the aerosol mass comprises of particles with diameters < D_{50}. The MMD offers a simple measure of particulate size distribution, albeit admittedly incomplete without consideration of the GSD. However, the reader is reminded of the results summarized in Table 3.1 where the GSD for all active seeding tests was approximately 2. The right side of Figure 3.9 shows the integrated transmission fraction as a function of average upstream MMD. Excluding the 350 kPa tests (red circles), it appears there may be an inverse relationship between transmission fraction and upstream MMD. The left side of Figure 3.9 shows the integrated transmission fraction as a function of the pressure drop across the microchannel. Excluding the 800 kPa test (yellow triangle), this plot indicates a positive relationship between transmission fraction and pressure differential. It stands to reason that aerosol transmission is influenced by both the pressure driving the flow and the size distribution of the aerosols in question, but additional testing is needed to establish the hierarchy of influence. From the plots below, it appears that 350 kPa of upstream pressure does not generate enough driving force for transport of larger particles through the microchannel. Although an upstream pressure of 800 kPa offers the greatest driving force, the transmission decreased due to the average upstream MMD being the largest in the dataset.

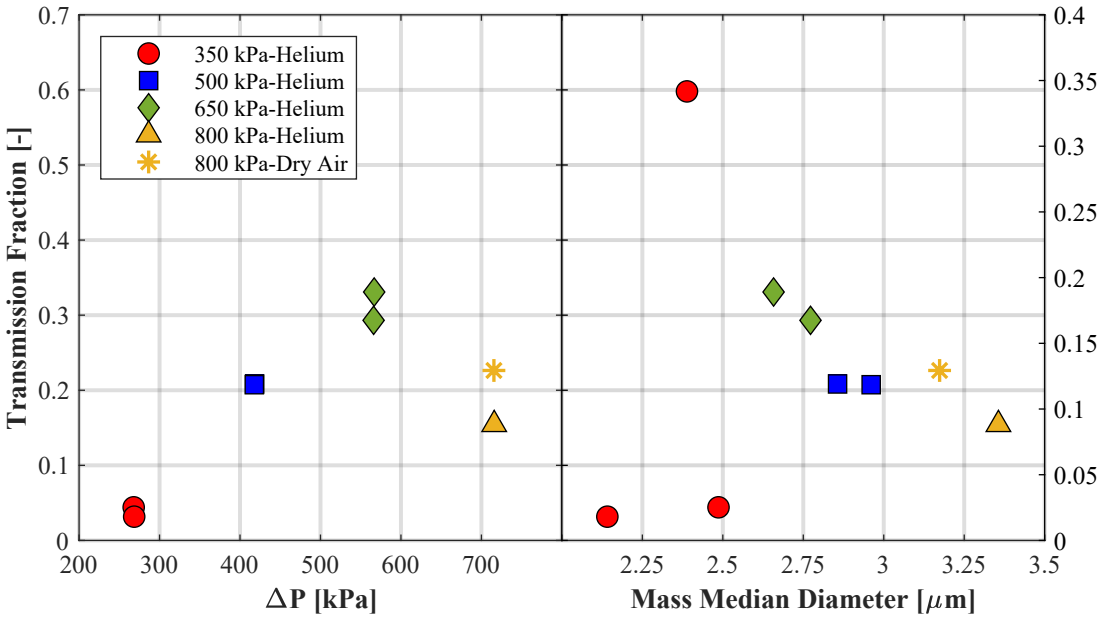

Figure 3.9 Integrated transmission fraction as a function of differential pressure across the microchannel (Left) and integrated transmission as a function of average upstream mass median diameter (right).

For testing in FY23 priority was given to using helium as the process fluid because it is the same gas used in actual DPCs. Due to current helium supply constraints, future testing will use dry air more extensively. A full test series using dry air has not yet been completed, but one test at 800 kPa using dry air was conducted and is included in these results. Although the authors are reluctant to draw conclusions from a single data point, the results appear to be similar to that of helium.

3.2.2 FY22 versus FY23 Testing Comparisons

The move to active seeding of the pressure tank throughout the course of the test resulted in reduced aerosol transmission across all pressure ranges. Figure 3.10 shows a comparison of FY22 data without active seeding and FY23 data with active seeding. FY22 tests resulted in transmission fractions in excess of 80% in some cases whereas FY23 had a maximum value of just over 30%. This result is not unexpected given that the microchannel is more effective at screening out larger particles than smaller particles. Active seeding results in overall larger particle size distributions throughout the duration of the test compared to blowdown testing in which near exponential decay of the size distribution occurs in the tank due to gravitational settling.

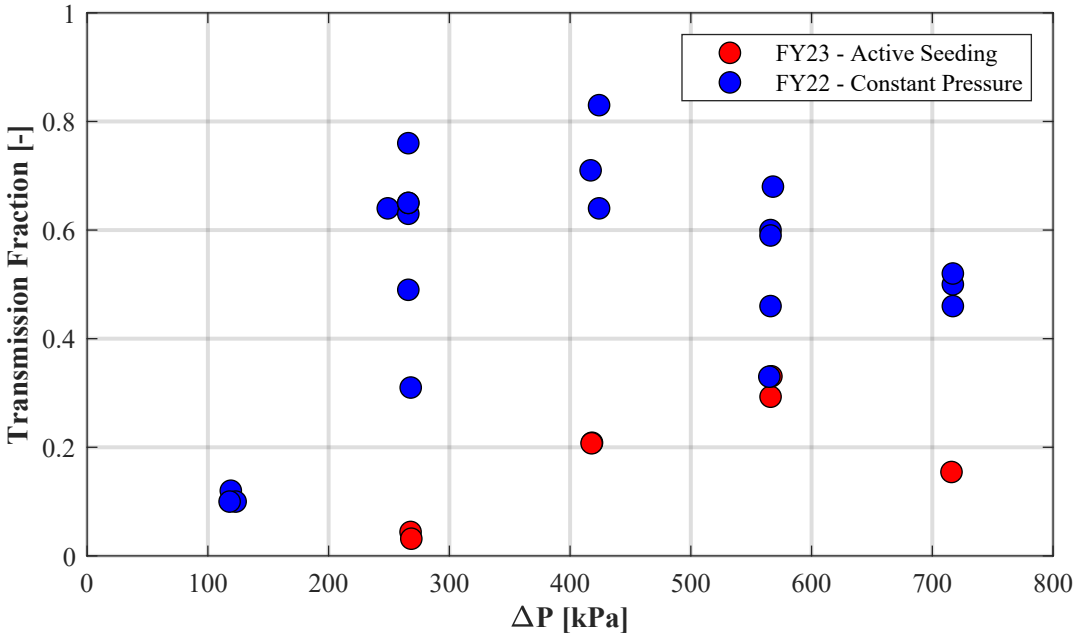

Figure 3.10 Comparison of FY22 and FY23 integrated transmission as a function of differential pressure across the microchannel with helium as the carrier gas.

Figure 3.11 shows a comparison of two tests at 500 kPa tests, where the test in FY23 used active seeding, and the test in FY22 used pre-test seeding. The exponential decay of the upstream and downstream MMD in the FY22 test is evident in Figure 3.11. The faster rate of decay in the upstream MMD reduces the mass concentration upstream faster than the reduction downstream, and instantaneous transmission increases during the test. Also noted is the increased MMD magnitude in the case of active seeding compared to the initial MMD with pre-test seeding, which was one of the primary motivations for the move to active seeding. The estimated particle size distribution from spent fuel testing MMD_o = 3.46 µm [Hanson *et al.*, 2008] was very hard to achieve in prior years without the ability to seed the pressure tank at the desired operating pressure due to the unavoidable delay between tank seeding and test initiation, the time required to raise the tank pressure to the desired operating pressure. During this period larger particles settle more rapidly than smaller ones, which decreases the aerosol size distribution and reduces the mass concentration.

The average MMD for the 500 kPa test on 7/5/2023 was 2.86 µm, which is much closer to the desired 3.46 µm than the FY22 initial MMD of 1.3 µm. While the seeding procedure has been simplified with the ability to seed at operating pressure, achieving a target size distribution in the upstream portion of the test section is still not entirely straightforward. The particle size distribution in the tank is monitored during initial seeding, but the eventual flow into the upstream test section once the 2-inch valve is opened shows reduced MMD compared to the tank. Efforts will continue to refine the tank seeding procedures to further increase MMD and hopefully attain more consistency as well.

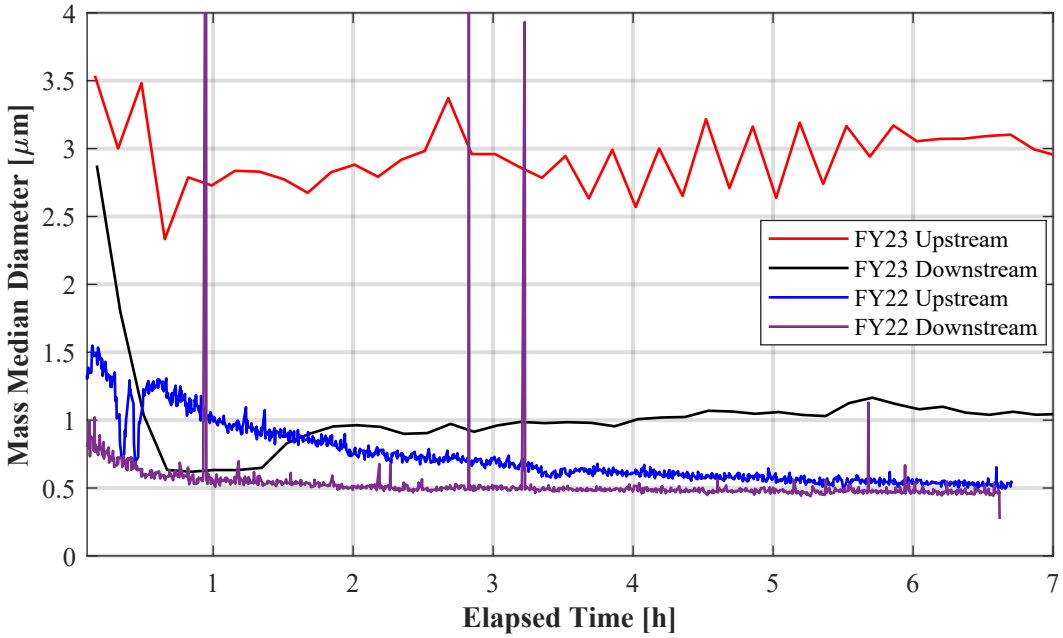

Figure 3.11 Comparison of MMD as a function of time between FY23 with active seeding (500 kPa – 7/5/23) and FY22 with pre-test seeding (500 kPa – 4/22/22).

Shown in Figure 3.12 is a comparison of FY22 and FY23 integrated transmission fraction as a function of MMD. Initial MMD (first 720 seconds) is used for the FY22 data, and average MMD over the course of the test is used for the FY23 data. Given the previously noted tendency for transmission fraction to decrease as MMD increases, it is not surprising that active seeding, which produces larger upstream aerosols, resulted in lower transmission rates.

Interestingly, the FY23 tests at 350 kPa resulted in significantly reduced transmission, which was not observed in FY22. A modest reduction in transmission could be explained by the larger particle sizes in FY23, but a decrease in excess of 90% is indicative that another mechanism is impacting the transmission fraction. This significant reduction was observed in FY22 in the case of the helium tests at 200 kPa, called out in Figure 3.12. It was previously thought that the decrease was caused by the use of a cover gas supplied to the exhaust portion of the facility which was required because the flow through the microchannel is less than the flow required to operate the downstream Welas sensor. It was postulated that the cover gas resulted in stagnation in the downstream portion of the test section and allowed for particles to settle prior to reaching the inlet for the Welas sensor. Given that the FY23 tests at 350 kPa did not require a cover gas yet also showed similar reduction in transmission fraction, a similar physical mechanism could be the cause in the FY22 tests at 200 kPa.

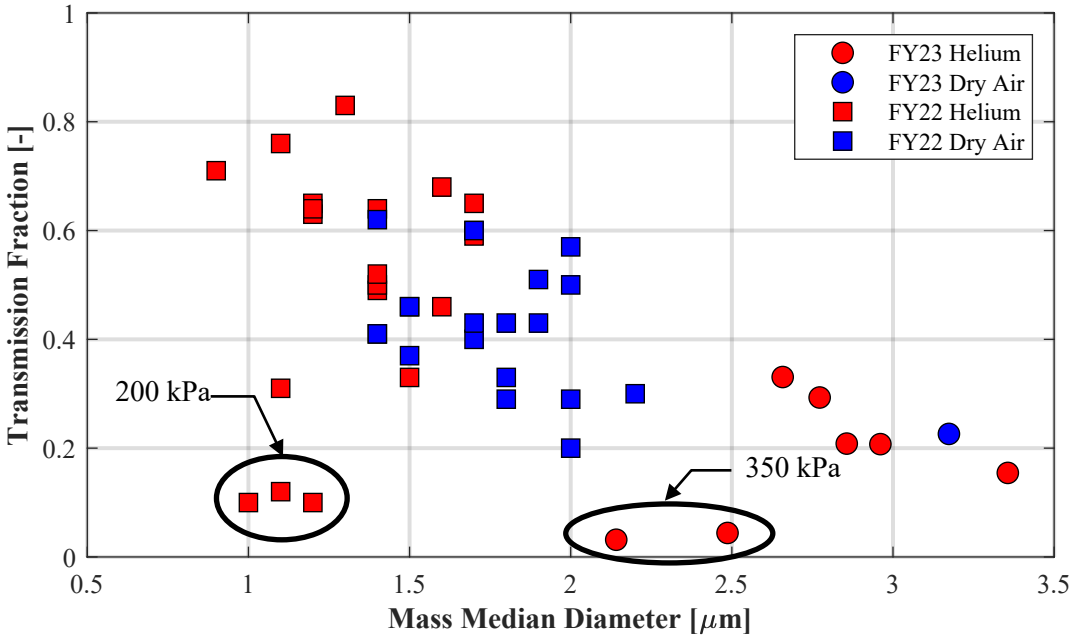

Figure 3.12 Comparison of FY22 Transmission as a function of initial MMD, and FY23 transmission as a function of average MMD.

The fact that significantly reduced transmission was observed for the lowest upstream pressures investigated indicates that there may be dependence of transmission on the differential pressure across the microchannel. This would be an intuitive conclusion except by in large the results from prior testing points to MMD as the dominant dependent variable.

For particles to be swept into the crack and transported to the downstream test section, they must traverse the length of the upstream test section from the tank to the crack and be swept into the crack by the developed accelerating flow to the crack inlet. Both of these mechanisms would exhibit upstream pressure dependence upon transmission fraction. Particle velocity in the upstream section would have a horizontal component from the free stream velocity and a downward component from the acceleration of gravity. Closer to the crack inlet, the flow accelerates towards the crack and could loft some particles towards the crack. Figure 3.13 illustrates the potential for horizontal average flow velocity to effectively screen out particles of different diameters. The black line represents the time of flight for particles falling at terminal velocity to traverse a distance of about 5 cm (the upstream pipe radius). The horizontal lines represent the time required for the flow to traverse about 30 cm (the length from the Welas sample port to the crack) moving at the bulk averaged flow velocity at upstream pressures of 200, 350, 500, 650, and 800 kPa. This plot is an oversimplification but illustrates the potential for settling of larger particles in the upstream test section, especially at lower upstream pressures. The implication of this effect is that particles that settle between the upstream sample port and the crack will calculate to reduced transmission fraction but in actuality would be removed by settling and not the crack. Although the significant drop in transmission was not seen in the FY22 350 kPa results, the much larger upstream size distribution in FY23 may be the reason for the apparent decrease. This effect could also be the cause for the decrease noticed in the FY22 200 kPa results.

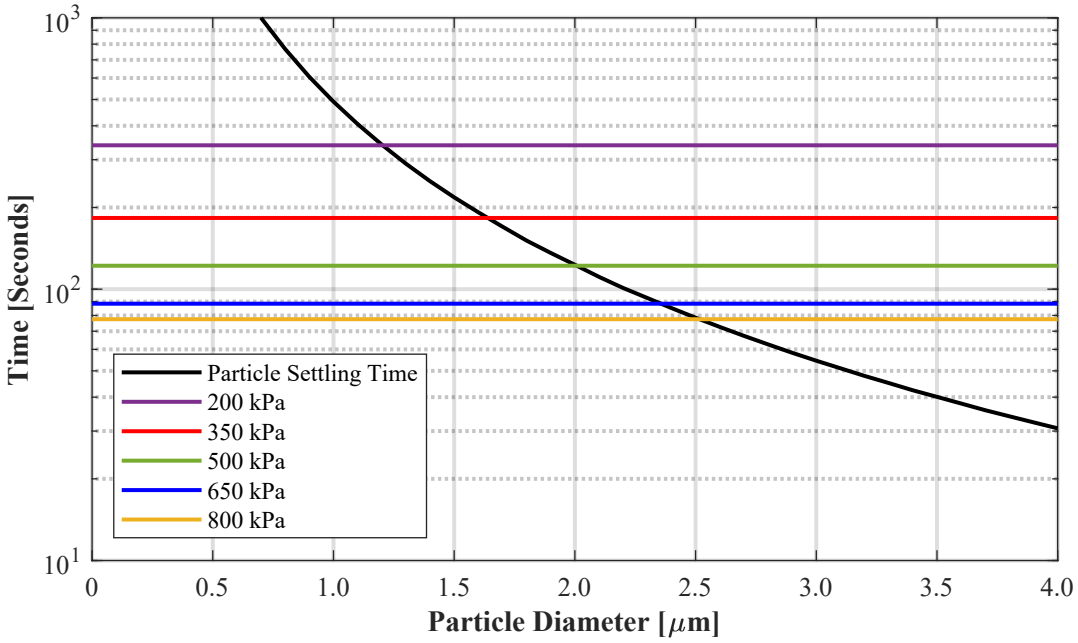

Figure 3.13 Time of flight for a particle to fall a distance of the pipe radius at terminal velocity (black), and time to traverse 12-inches at different upstream pressures at average horizontal flow velocity.

Aerosol-laden flow testing with the use of microchannels has not only provided useful information and insight into the behavior of aerosol transport through crack-like geometries but has also served as an effective test bed for facility operability and test procedures. Future testing will involve aerosol-laden flow testing of lab-grown SCCs, such as the EPRI cracks detailed in Section 2.3 and the SNL lab-grown cracks in development detailed in Section 4.2.1, which are expected to foul during testing and are limited to a single use. The lessons learned during the execution of microchannel testing will help to ensure limited lab-grown crack resources are not wasted.

This page is intentionally left blank.

4 Future Work

4.1 Continuation of Microchannel Testing

Continued testing of the diverging microchannel with active seeding of particulates is planned for the future. The active seeding procedure is planned to be further refined throughout the dry air testing series to increase control over the upstream particle size distribution.

The benefit of testing with the linearly diverging microchannel is the well-defined and understood crack geometrical parameters. The main drawback with a simple slot orifice or diverging crack is that there is no tortuosity in the flow path as is expected in a real SCC. It is possible that the tortuous path of a SCC will result in particulate deposition, accumulation, or even partial plugging of the flow path. To better understand the potential for and effects of particulate build up, microchannels with manufactured tortuosity, such as the examples shown in Figure 4.1, are intended to be designed and manufactured for aerosol-laden flow testing. Aerosol accumulation or plugging in a manufactured re-useable crack with well-defined tortuosity can provide valuable data for collaborative modeling efforts [Chatzidakis and Sasikumar, 2021] attempting to model such phenomena.

Figure 4.1 Concepts for microchannel geometries with manufactured tortuosity.

4.2 Lab-Grown Stress Corrosion Cracks

Although the engineered microchannel used for flow testing in this report has characteristic dimensions of a SCC, it fails to capture the tortuosity and dendritic structure representative of an actual through-wall crack. The aerosol-laden flow testing results with the engineered microchannel presented in Section 3.2 have proven useful for model validation and experimental capability verification. The next logical approach was to incorporate an actual stress corrosion crack into the test setup and procedures that have been developed for aerosol seeding and transmission at SNL. As described in Section 3.1, two plates with through-wall stress corrosion cracks from EPRI, see section 2.3, have been characterized and used for clean flow testing. SNL is also attempting to prepare through-wall SCC specimens for mitigation and repair techniques and aerosol-laden flow testing. Three things are required for SCCs to develop, a material that has the potential to undergo corrosion, elevated tensile stress in the specimen, and exposure to a corrosive species. The primary difference in the methodology used to develop a lab-grown crack between the EPRI cracks and the SNL cracks is the means by which tensile stress is developed in the specimen. EPRI placed their specimens in a 3-point bending apparatus generating the stress via mechanical fixation, whereas SNL did so by welding the specimen which generates the tensile stress as the heated material contracts as it cools. The benefit of welding is that the tensile stress is developed through the thickness of the sample compared to only half the sample in the case of bending. The SNL methodology will hopefully lead to SCC samples with a total material thickness closer to DPC canister shells. Nonetheless, the SCC plates from EPRI will provide a good comparison to microchannel and SNL lab-grown crack testing.

4.2.1 SNL Lab-Grown SCC

SNL is developing their own procedure to rapidly grow cracks under controlled laboratory settings for SCC flow studies and for mitigation and repair experiments. The SNL cracks will also be more representative of a crack through a SNF canister shell compared to the engineered microchannel and EPRI crack samples. The tensile stresses imposed on the EPRI plates were from an external load, whereas the tensile stresses present in the canister shell are internal to the material. The residual tensile stresses in a SNF canister are an artifact of the welds during fabrication. As the weld cools, the filler metal contracts, introducing significant tensile stresses in the weld regions of the canister. A previous investigation of SCCs indicated that the stresses around the weld region were found to be strongly tensile throughout the thickness of the canister shell [Enos and Bryan, 2016]. SCCs are anticipated to initiate and propagate in these regions of significant tensile stress, given the presence of a corrosive environment. The SNL lab-grown cracks will attempt to replicate these internal stresses prior to introducing an aggressive salt solution to the material's surface.

4.2.1.1 Previous Attempts

The residual stresses from welding a circular plug into a larger plate have been investigated and should provide sufficient tensile stresses to form and grow a stress corrosion crack. Three attempts to form a SCC after this welding operation have been conducted at SNL, one of which yielded an observable through-wall SCC. One reason for being unsuccessful was the lack of adherence to fabrication guidelines. A haphazard weld job caused noticeable voids in the weld and a weld that was not uniform through the thickness of the material. One of the plates is shown in Figure 4.2. With the lack of a full-penetration weld, the stress field around the weld was not entirely representative of a welded SNF canister.

Figure 4.2 Bottom side of completed circular weld plate for laboratory-grown stress corrosion crack (left) and experimental setup for chloride-induced stress corrosion crack growth (right).

Despite unsatisfactory fabrication of the plates, SNL researchers attempted to grow cracks using a magnesium chloride solution, shown in Figure 4.2. The magnesium chloride solution was saturated at room temperature and exposed to the material surface for several weeks. The chloride solution provided the corrosive environment for an SCC to initiate. A hot plate was used to maintain a temperature between 100 and 110 °C. This temperature range is indicative of a SNF canister that has been in service for several years and may begin to show signs of aging.

As stated previously, one of the three attempts to induce a through-wall SCC was successful. An image of the laboratory-grown crack is shown in Figure 4.3. This plate is slated to be used for exploring different coatings as a SCC repair technique.

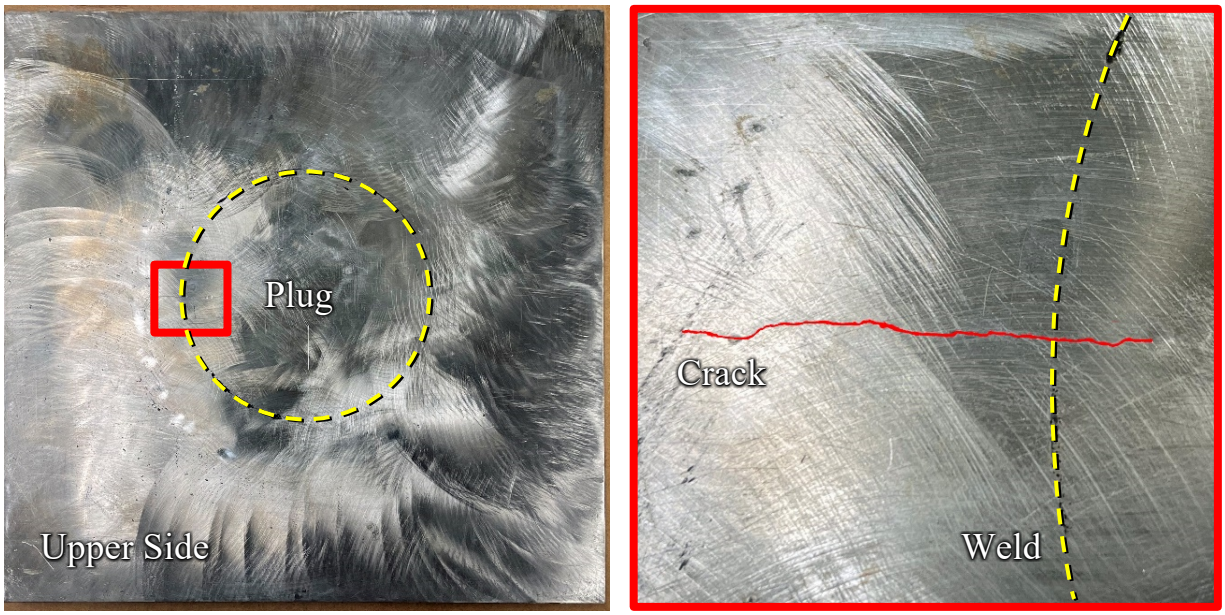

Figure 4.3 Successful through-wall SCC grown with welded plate at SNL.

4.2.1.2 Current Fabrication Methodology

The current fabrication process for the plates follows a more stringent procedure than the previous attempts. A 127 mm (5.0 in.) diameter plug was waterjet-cut from a 12.7 mm (0.50 in.) thick 292 mm (11.5 in.) diameter 304L stainless steel plate, shown in Figure 4.4. Also shown in Figure 4.4, is the welding progression of the plate. First, the top (inner) side of the plate was welded into place entirely. The fabricator then flipped the plate over and back-gouged the plate, removing material down to the initial root weld. This process ensures a full-penetration weld. Finally, the bottom (outer) side of the material was welded. An experienced welder would likely switch between each side to be welded to reduce the residual stresses in the material and limit the risk of warping and deformation. SNF canisters are not constructed in this manner, however, and strong tensile stresses are favorable for SCC growth. For this reason, the current plates have been welded one side at a time.

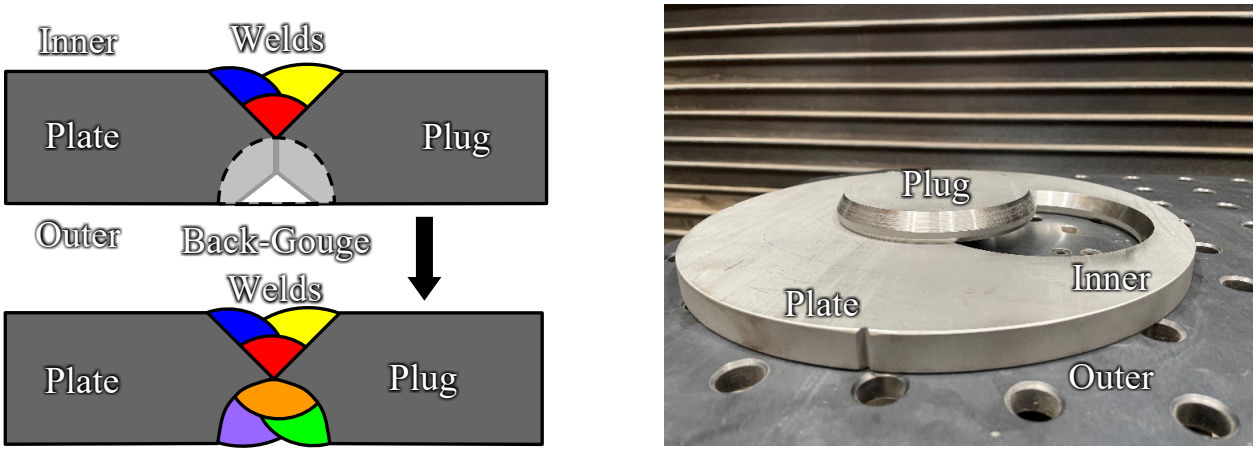

Figure 4.4 Welding fabrication steps (left) and waterjet-cut plate and plug (right).

After welding and prior to crack growth, a 4-in. flange bolt pattern will be cut into the welded plate. This will allow for the plate to be mounted on the current experimental setup, replacing the engineered microchannel, for flow testing. This sequence of processes was chosen because cutting the flange holes after crack growth could contaminate and potentially clog the crack. A computer model of the finished plate, with a stress corrosion crack, is shown in Figure 4.5. The mounting of the plate is similar to the current procedure, using rubber gaskets to seal and torquing the bolts to 120 N·m (90 ft·lbf). Exploded and assembled depictions of the crack plate mounted on the 4-in. flanges of the test section is shown in Figure 4.6.

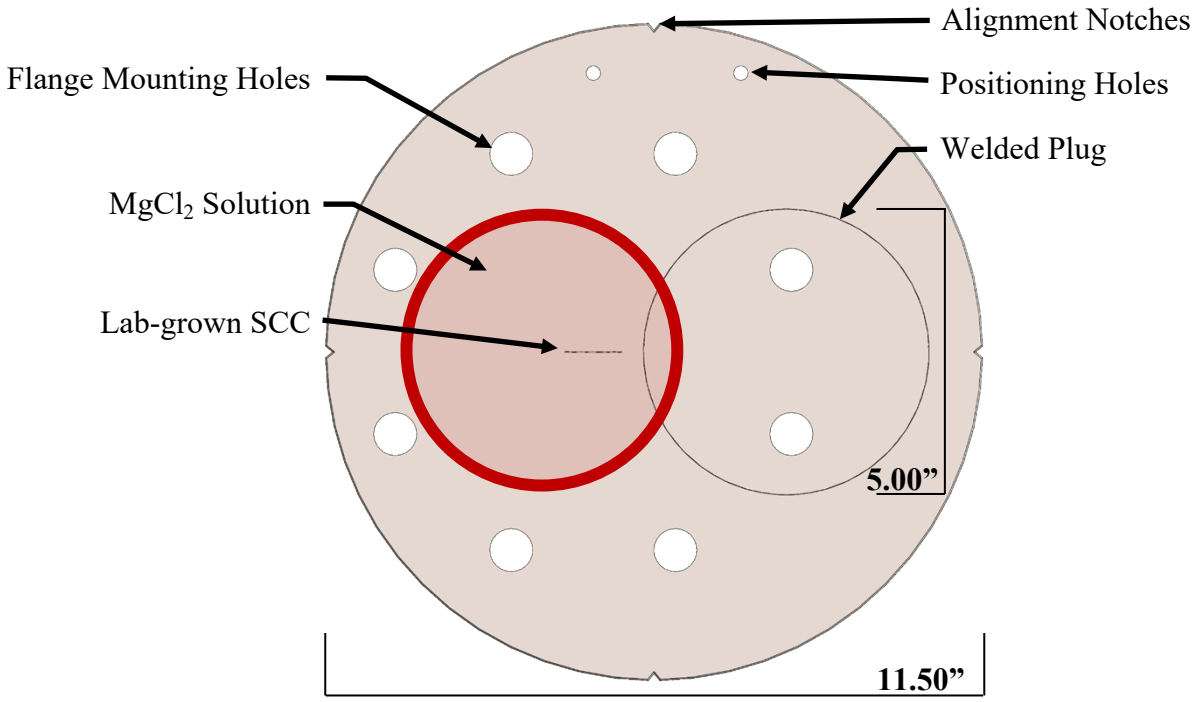

Figure 4.5 Computer-aided design of mountable stress corrosion crack plate.

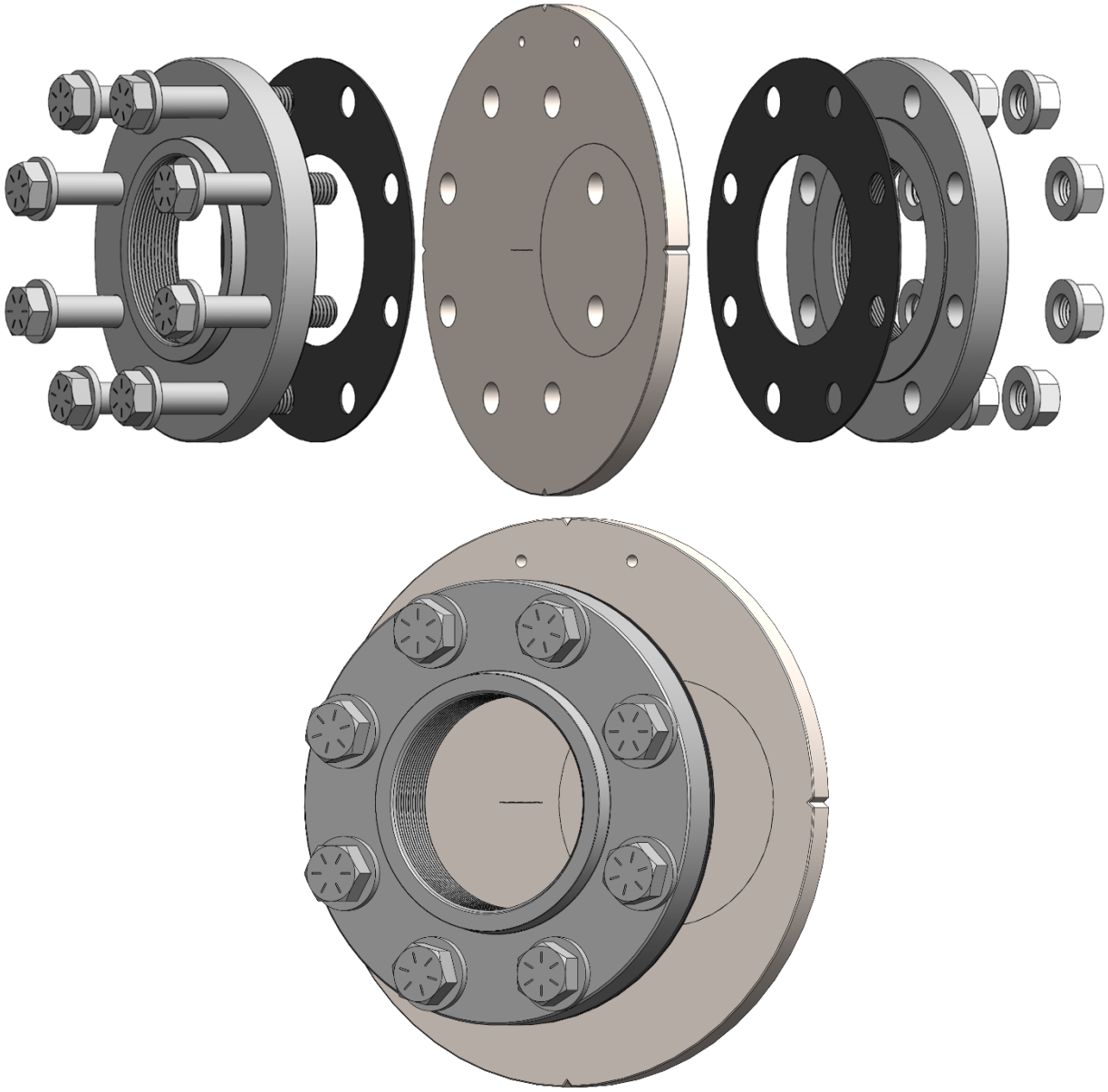

Figure 4.6 Exploded (top) and assembled (bottom) models of the mountable lab-grown SCC assembly capable of being implemented into the current test setup shown in Figure 2.3.

4.2.1.3 Fabrication Process

Two plates have been made prior to growing a SCC to determine if the fabrication process is satisfactory and imposes sufficient residual tensile stresses within the plate. The initial welding setup and welding of the plate are shown in Figure 4.7. The first and last weld passes of the "inner" side are shown in Figure 4.8.

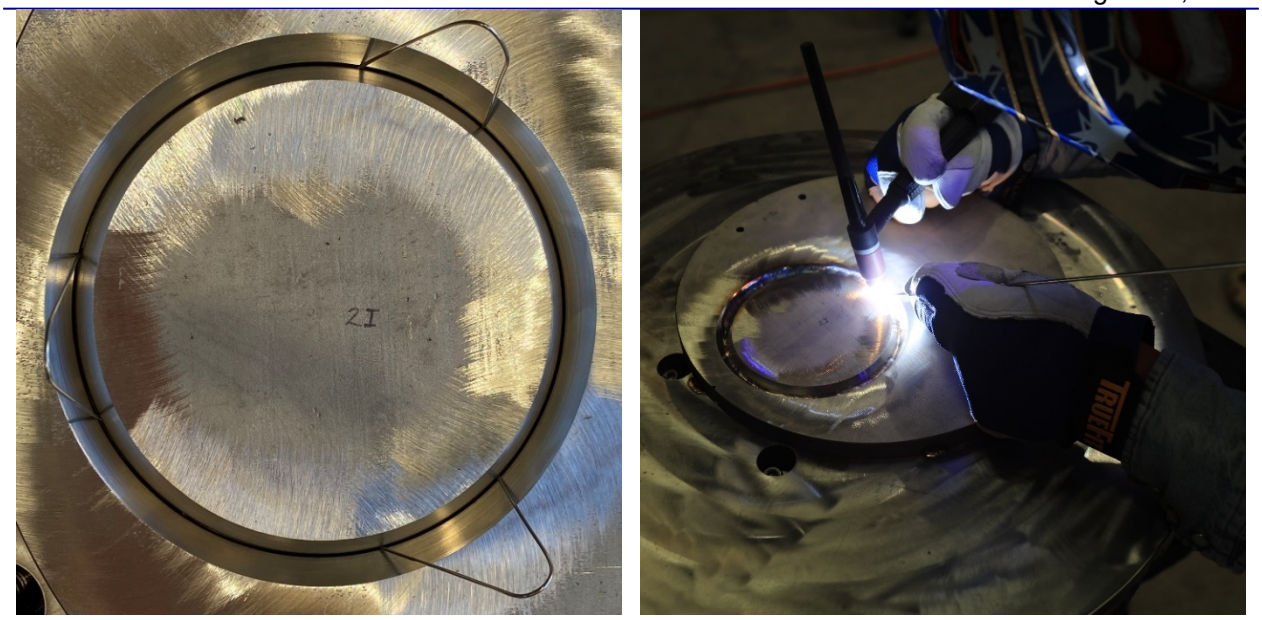

Figure 4.7 Initial welding setup to ensure plug concentricity (left) and welding of the plug in place (right).

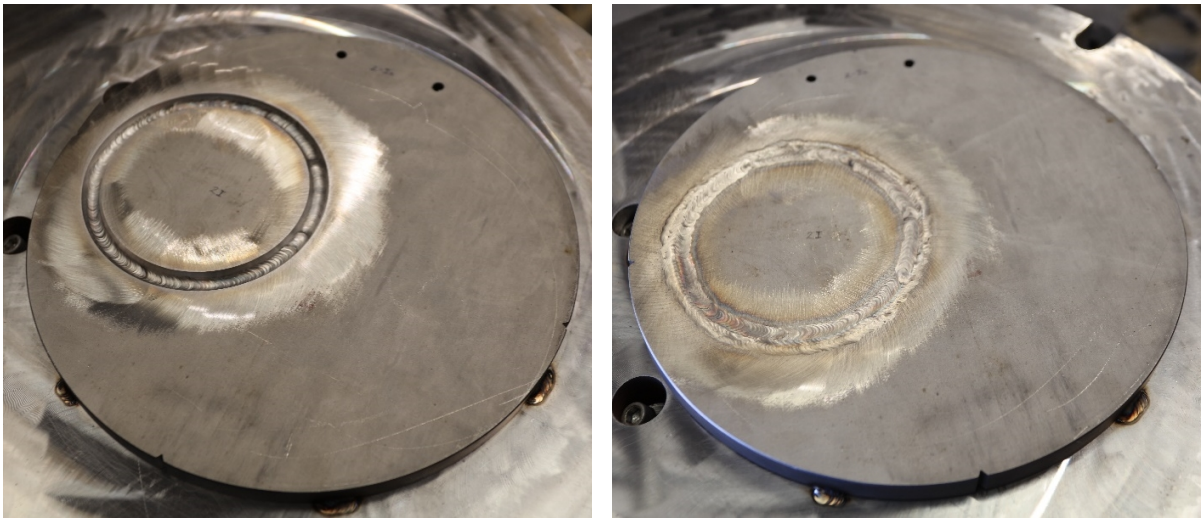

Figure 4.8 First (left) and last (right) completed weld passes on the "inner" side of the plate.

To limit the chance of warping, the plate was tack-welded to a larger stainless steel plate during welding. Upon completion of the final weld pass, however, the large internal stresses in the plate caused the plate to warp, breaking the tack-welds securing it to the larger plate. An image of this deformation is shown in Figure 4.9. The second plate welded received larger tack welds, which did not break, but the plate still warped after the tacks were cut away to weld the other side of the plate. The initial and final appearances of the welded "outer" side of the plate are shown in Figure 4.10.

Figure 4.9 Significant internal stresses after welding caused considerable deformation in the plate, breaking the tack welds holding it in place.

Figure 4.10 SCC plate before (left) and after (right) welding the "outer" side.

The plate must be flat to form a proper seal during flow testing. Due to the warping in the plates, they had to be planed down on a mill. A shell mill, shown in Figure 4.11, was used for planing the top and bottom surfaces of the plate. The plate after all welding, machining, and polishing operations is shown in Figure 4.12. The final thicknesses of the plates are approximately 9 mm (0.35 in.); more representative of a SNF canister than the EPRI plates. The plate has been passed off to grow the SCC for flow testing. Cracks grown in this manner are planned to be the most representative of a through-wall SCC on a SNF canister to date. Clean flow and aerosol-laden flow data will be invaluable in understanding the amount of particulate transmission possible in a scenario where there is loss of containment.

Figure 4.11 End mill was used to plane down the surface of the plate, removing the deformation caused by welding.

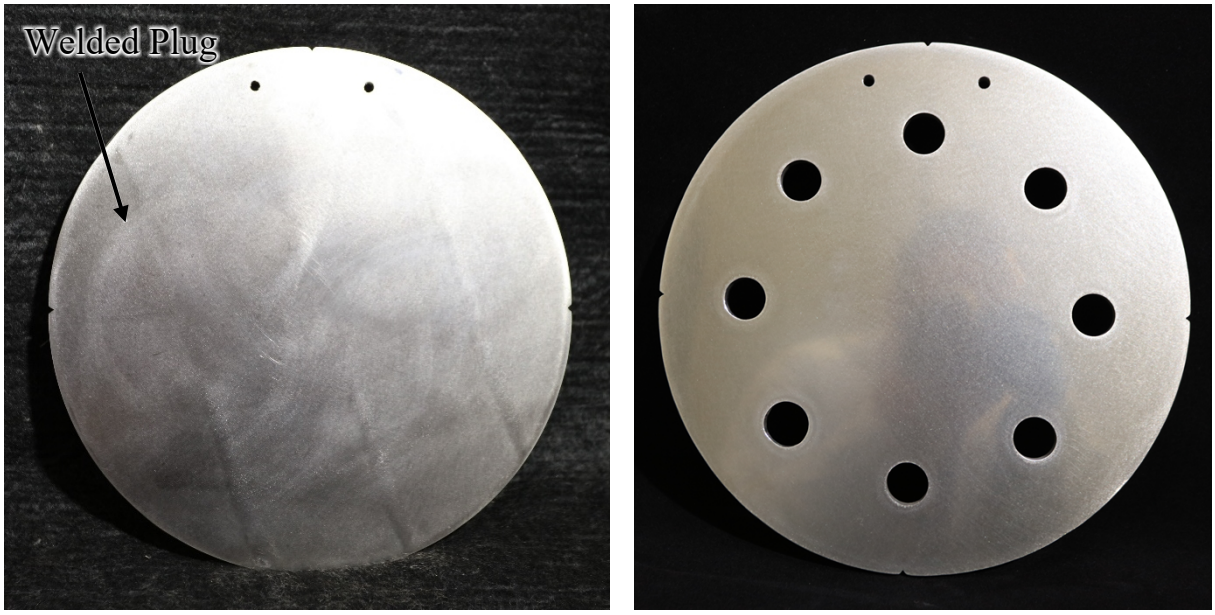

Figure 4.12 Finished SCC plate after welding and machining operations.

5 SUMMARY

5.1 Microchannel Testing

Using a microchannel with an initial cross-section of 12.7 mm × 13 μm tapering linearly to 12.7 mm × 25 μm and a flow length of 8.86 mm, a total of nine aerosol-laden constant pressure with active seeding tests were conducted at four nominal upstream pressures (350 kPa, 500 kPa, 650 kPa, and 800 kPa). Tests were conducted with helium as the backfill gas. This microchannel represents the typical dimensions of an SCC albeit without any tortuosity and is therefore a relatively conservative simplification of a hypothetical SCC in a dry storage canister for SNF. The pressure in the tank was maintained through the use of a pressure controller to establish a constant pressure differential across the micro-channel. Previous testing [Durbin *et al*., 2021] showed that because aerosol mass transmission largely occurred at the beginning of the tests, there was no discernable difference in the transmission between the blowdown tests and the tests conducted at constant pressure. As such, subsequent testing focused on constant pressure tests to decouple the SCC discharge characteristics from the pressure transient [Jones *et al*., 2022]. Prior years testing continually alluded to the upstream MMD being the primary factor which affected the transmissibility of aerosols across a microchannel. To further improve understanding of the influence of upstream MMD, the ability to actively seed the pressure tank was pursued and development of this capability and results of testing are presented in this report. Actively seeding the pressure tank resulted in an increase in the particle size distribution throughout the test duration across all upstream pressure conditions. Because larger particles transport through the crack less effectively, the transport fraction is also reduced across all pressure conditions. A significant decrease in transmission was shown in tests at 350 kPa upstream pressure. This could be caused by particulate settling as the flow traverses the distance of the upstream test section, and the effect would be more pronounced given the greater upstream particle size distribution compared to prior years testing. Global helium supplies remain strained and actively seeding increases helium consumption by a large margin, so a dry air test series is planned.

5.2 Lab-Grown Crack Testing

In moving towards even more prototypic crack geometries, two lab-grown crack samples were provided to SNL by EPRI. These cracks will ultimately be used for aerosol-laden flow testing, but baseline clean flow testing with dry air and helium was conducted and is presented in this report. The morphology of the crack is expected to influence both the flow of the carrier gas through the crack and the potential for particulate to accumulate in the crack. Initial non-destructive efforts to characterize the EPRI cracks have been conducted, presented in Section 2.3, which evaluated crack dimensions using optical techniques. The thickness of the crack samples are not prototypic at roughly 1/4th the thickness of a canister shell because they were produced for mitigation and repair testing and not flow testing. The cracks are also expected to foul with particulate after a single aerosol laden flow test and will thus be single use only. For these two reasons, SNL is currently developing a procedure to produce lab-grown SCC samples and progress is reported in Section 4.2.1. Production of numerous samples will allow for the ability to conduct a statistically relevant number of tests, and the procedure will be improved to produce samples of adequate thickness. The SNL lab-grown SCCs could also be of use in other areas of research related to SCCs in DPCs and other collaborative opportunities are likely to arise.

This page is intentionally left blank.

6 REFERENCES

Casella, A., S.K. Loyalka, and B.D. Hanson, "Plugging Effects on Depressurization Time in Dry Storage Containers with Pinhole Breaches," **Trans. American Nucl. Soc.**, ***95***, 209-210, Washington, D.C., June (2006).

Casella, A., S.K. Loyalka, and B.D. Hanson, "Pinhole Breaches in Spent Fuel Containers: Improvements to Conservative Models of Aerosol Release and Plugging," **Trans. American Nucl. Soc.**, ***97***, 439-440, Washington, D.C., November (2007).

Chatzidakis, S., and Y. Sasikumar, "Progress Report on Model Development for the Transport of Aerosol through Microchannels," ORNL/SPR-2020/1599, Oak Ridge National Laboratory, Oak Ridge, Tennessee, April (2021).

Durbin, S.D., E.R. Lindgren and R.J.M. Pulido, "Measurement of Particulate Retention in Microchannel Flows", SAND2018-10522R, Sandia National Laboratories, Albuquerque, New Mexico, September (2018).

Durbin, S.G., E.R. Lindgren, and A.G. Perales, "Estimation of Respirable Aerosol Release Fractions through Stress Corrosion Crack-Like Geometries," SAND2020-9014R, M2SF-20SN010207016, Sandia National Laboratories, Albuquerque, New Mexico, August (2020).

Durbin, S.G., R.J.M. Pulido, E.R. Lindgren, P.G. Jones, H. Mendoza, and J. Phillips, "Continued Investigations of Respirable Release Fractions for Stress Corrosion Crack-Like Geometries," SAND2021-9222R, M2SF-21SN010207071, Sandia National Laboratories, Albuquerque, New Mexico, July (2021).

Enos, D. and C. Bryan, "Final Report: Characteriszaton of Canister Mockup Weld Residual Stresses," SAND2016-12375R, Sandia National Laboratories, Albuquerque, New Mexico, November (2016).

EPRI, "Flaw Growth and Flaw Tolerance Assessment for Dry Cask Storage Canisters," EPRI 3002002785 Electric Power Research Institute, Palo Alto, CA, October (2014).

EPRI., "Dry Cask Storage Welded Stainless Steel Canister Breach Consequence Analysis Scoping Study," EPRI 3002008192, Electric Power Research Institute, Palo Alto, CA, November (2017).

EPRI., "Investigation of Advanced Coating Technologies for Mitigation of Chloride-Induced Stress Corrosion Cracking," EPRI 3002023825, Electric Power Research Institute, Palo Alto, CA, November (2022).

Faubel, J.L., "Characterization of Lab-Grown Cracks for Aerosol Transmission Testing", SAND2023-12180R, M3SF-23SN010207063, Sandia National Laboratories, Albuquerque, New Mexico, February (2023).

Gelbard, F., and S. G. Durbin, "Aerosol Particle Deposition on a Spent Nuclear Fuel Assembly Spacer Grid," SAND2023-02079R, M2SF-23SN010207064, Sandia National Laboratories, Albuquerque, New Mexico, April (2023).

GOTHIC, "Thermal Hydraulic Analysis Package, Technical Manual," (2018).

Hanson, B.D., R.C. Daniel, A.M. Casella, R.S. Wittman, W. Wu (BSC), P.J. MacFarlan, and R.W. Shimskey, "Fuel-In-Air FY07 Summary Report," PNNL-17275, Pacific Northwest National Laboratory, Richland, Washington, September (2008).

Humphries L.L., *et al.*, "MELCOR Computer Code Manuals, Vol. 1: Primer and Users' Guide Version 2.2.11932," SAND2018-13559 O, November 2018.

Jones, P.G., R. J. M. Pulido, A. Perales, and S. G. Durbin, "Quantification of Aerosol Transmission through Stress Corrosion Crack-Like Geometries," SAND2022-11170R, M2SF-22SN010207074, Sandia National Laboratories, Albuquerque, New Mexico, August (2022).

Lanza, M., M. Leimon, M. Elsawi and A. Casella., "GOTHIC Aerosol Source Depletion Studies," PNNL-31176, M3SF-21PN 010207042, Pacific Northwest National Laboratory, Richland, Washington, April (2021).

Lanza, M., M. Leimon, and A. Casella., "Continued Studies on Aerosol Source Depletion in Dry Spent Nuclear Fuel Storage Canister with GOTHIC," PNNL-32794, M3SF-22PN010207042, Pacific Northwest National Laboratory, Richland, Washington, April (2022).

Lewis, S., "Solid Particle Penetration into Enclosures", J. Hazardous Materials, *43,* 195-216, (1995).

Liu, D-L.and W.W. Nazaroff, "Modeling Pollutant Penetration Across Building Envelopes," **Atmos. Environm**., ***35***, 4451-4462, (2001).

Liu, D-L. and W.W. Nazaroff, "Particle Penetration Through Building Cracks," **Aerosol Science and Technology**, ***37***, 565-573, (2003).

Meyer, R.M., S. Suffield, E.H. Hirt, J.D. Suter, J.P. Lareau, J.W. Zhuge, A. Qiao, T.L. Moran, and P. Ramuhalli, "Nondestructive Examination Guidance for Dry Storage Casks," PNNL-24412 Rev. 1, Pacific Northwest National Laboratory, Richland, Washington, September (2016).

Mosley, R.B., D.J. Greenwell, L.E. Sparks, Z. Guo, W.G. Tucker, R. Fortmann, C. Whitfield, "Penetration of Ambient Fine Particles into the Indoor Environment," **Aerosol Science and Technology**, ***34***, 127-136, (2001).

Nakos, J.T., "Uncertainty Analysis of Thermocouple Measurements Used in Normal and Abnormal Thermal Environment Experiments at Sandia's Radiant Heat Facility and Lurance Canyon Burn Site," SAND2004-1023, Sandia National Laboratories, Albuquerque, NM, April 2004.

NRC, "Spent Fuel Transportation Risk Assessment," United States Nuclear Regulatory Commission, NUREG-2125, May (2012).

Palas GmbH, "RBG 1000 Particle Generator Manual," Karlsruhe, Germany, (2002).

Phillips, J. and F. Gelbard., "Interim Report on Aerosol Deposition Inside a Spent Fuel Transportation and Storage Canister," SAND2021-5202R, M3SF-21SN010207072, Sandia National Laboratories, Albuquerque, New Mexico, April (2021).

Phillips, J., "MELCOR Input Model for Spent Fuel Transportation and Storage Canister," SAND2022-7306R, M3SFSN010207073, Sandia National Laboratories, Albuquerque, New Mexico, May (2022).

Powers, D.A., "Aerosol Penetration of Leak Pathways – An Examination of the Available Data and Models," SAND2009-1701, Sandia National Laboratories, Albuquerque, NM, April (2009).

Sanders, T.L., K.D. Seager, Y.R. Rashid, P.R. Barrett, A.P. Malinauskas, R.E. Einziger, H. Jordan, T.A. Duffey, S.H. Sutherland, and P.C. Reardon "A Method for Determining the Spent-Fuel Contribution to Transport Cask Containment Requirements," SAND90-2406, Sandia National Laboratories, Albuquerque, NM, November (1992).

Schindelholz, E., C. Bryan, and C. Alexander, "FY17 Status Report: Research on Stress Corrosion Cracking of SNF Interim Storage Canisters," SAND2017-10338R, Sandia National Laboratories, Albuquerque, NM, August (2017).

APPENDIX A TRANSIENT AEROSOL MASS CONCENTRATIONS

The tests presented in this appendix are defined by the test date, the nominal upstream pressure, and the fill gas (air or helium). The integrated upstream and downstream mass and transmission fraction is also provided.

A.1 Dry Air Tests

A.1.1 800 kPa Air

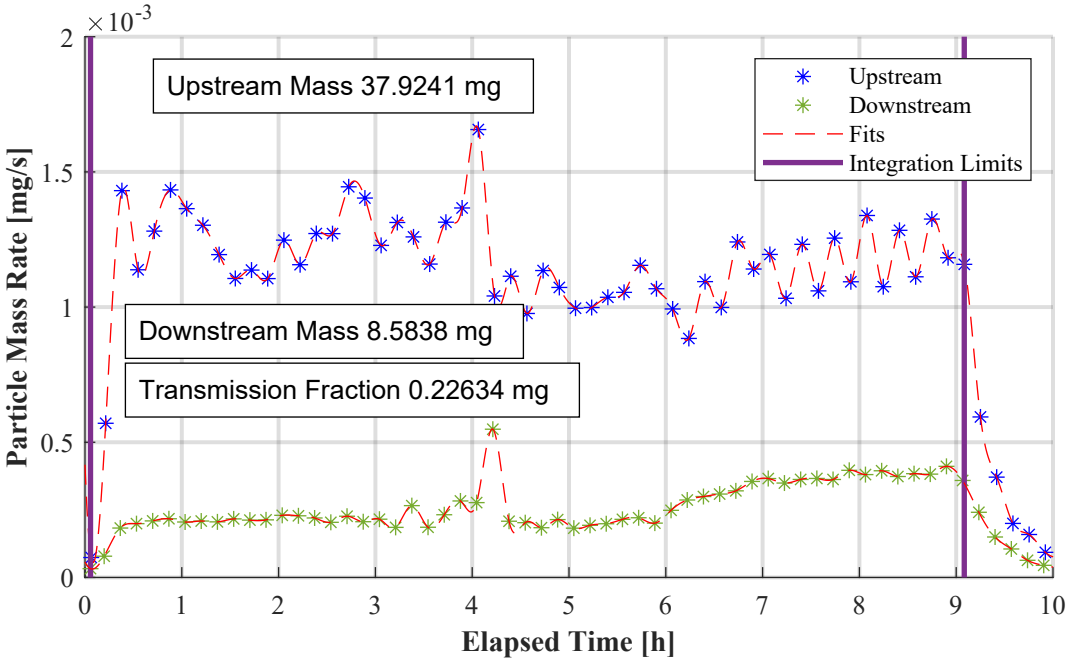

Figure A-6.1 Particle mass rate with spline fits for integration for the air test with active seeding conducted on 07/25/2023 with upstream pressure = 800 kPa.

A.2 Helium Tests

A.2.1 350 kPa Helium

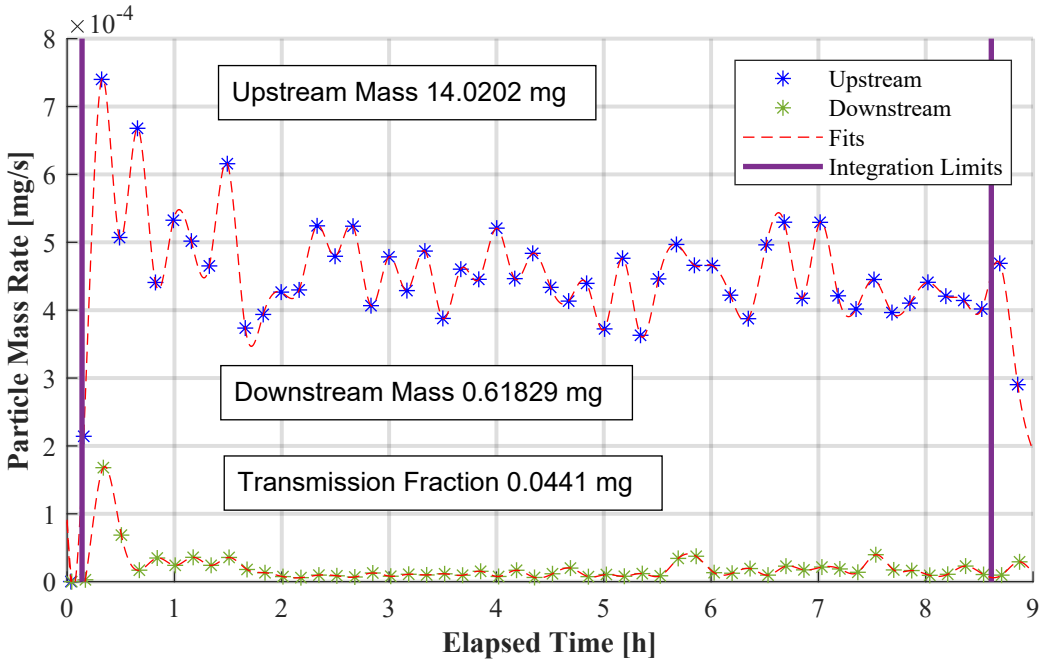

Figure A-6.2 Particle mass rate with spline fits for integration for the air test with active seeding conducted on 06/29/2023 with upstream pressure = 350 kPa.

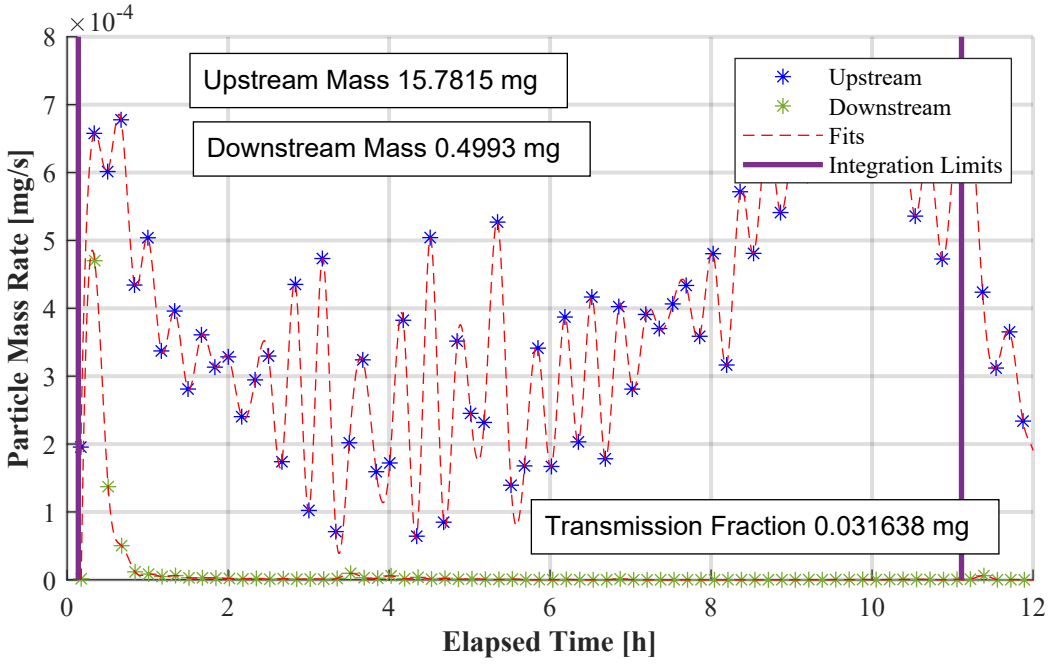

Figure A-6.3 Particle mass rate with spline fits for integration for the air test with active seeding conducted on 07/18/2023 with upstream pressure = 350 kPa.

A.2.2 500 kPa Helium

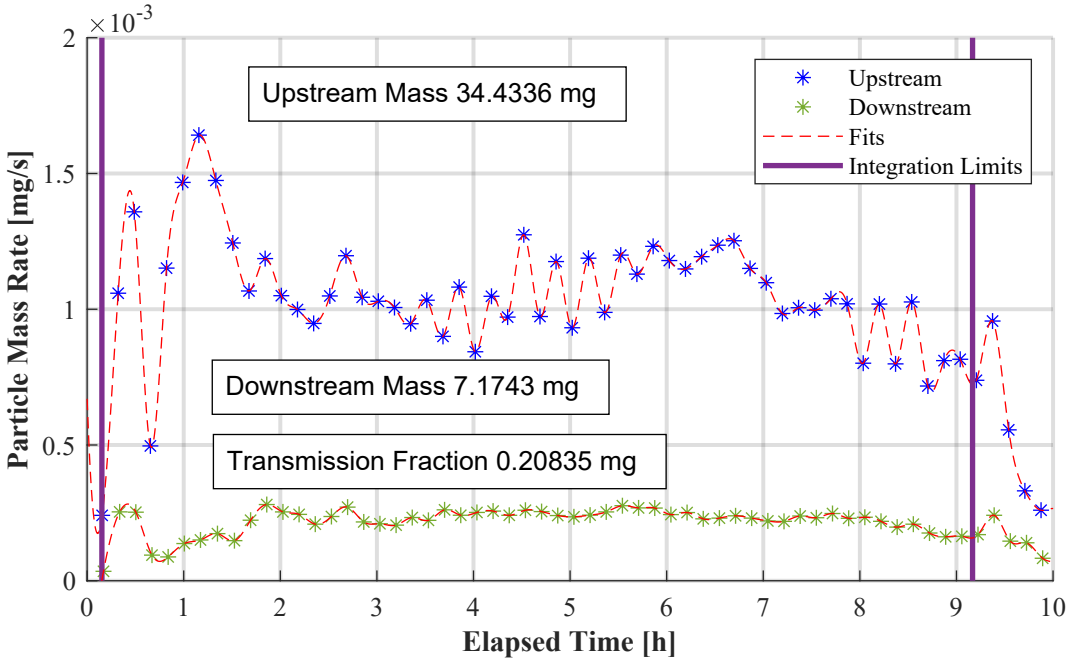

Figure A-6.4 Particle mass rate with spline fits for integration for the air test with active seeding conducted on 07/5/2023 with upstream pressure = 500 kPa.

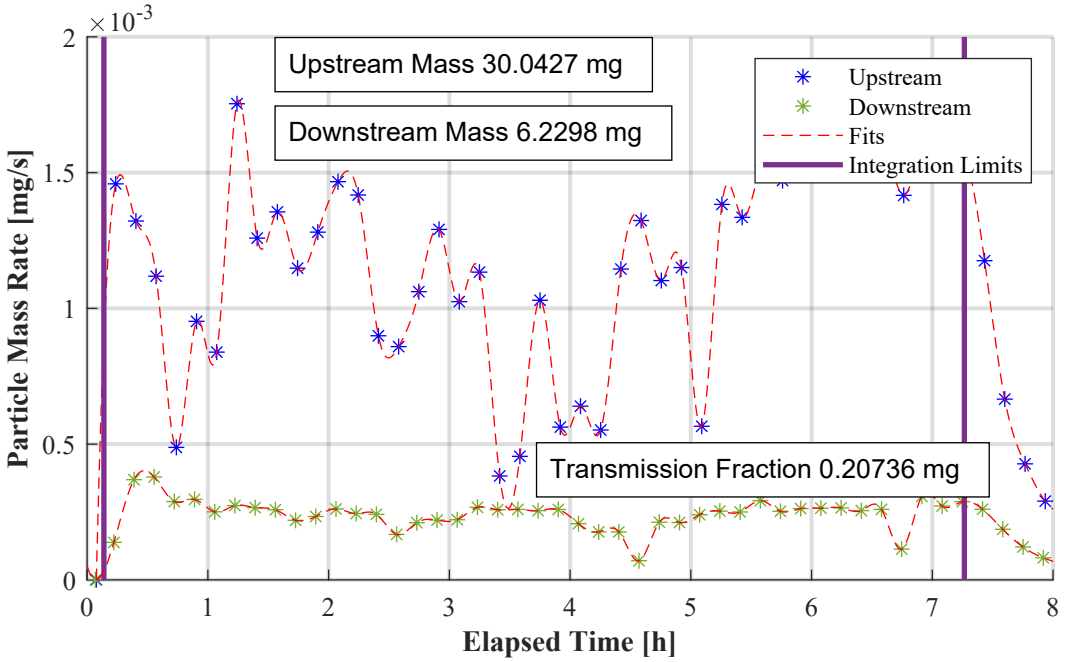

Figure A-6.5 Particle mass rate with spline fits for integration for the air test with active seeding conducted on 07/12/2023 with upstream pressure = 500 kPa.

A.2.3 650 kPa Helium

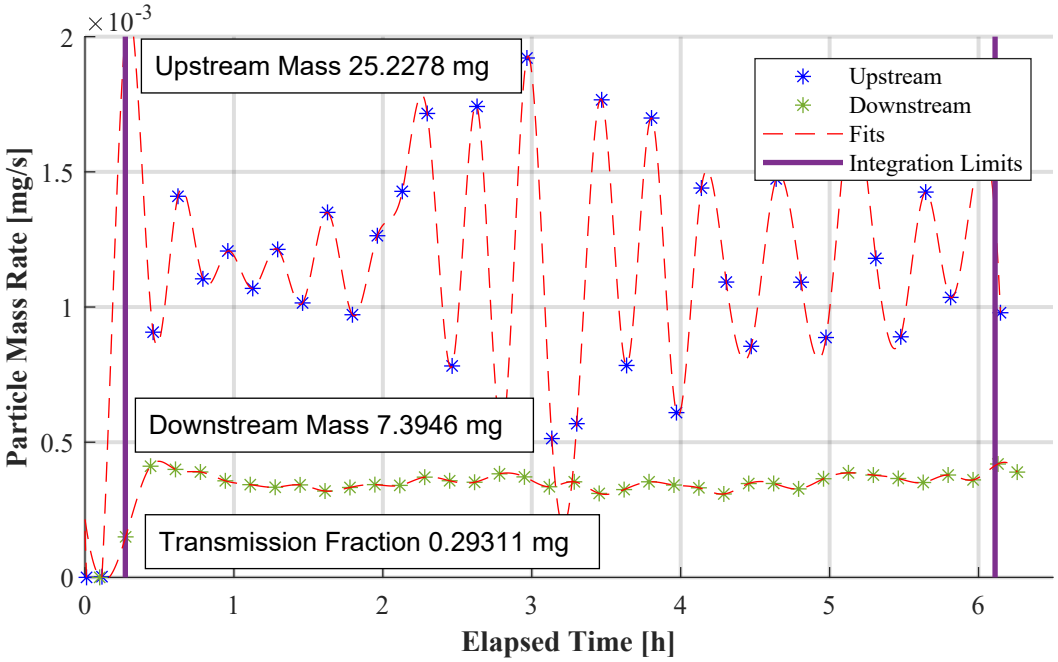

Figure A-6.6 Particle mass rate with spline fits for integration for the air test with active seeding conducted on 07/20/2023 with upstream pressure = 650 kPa.

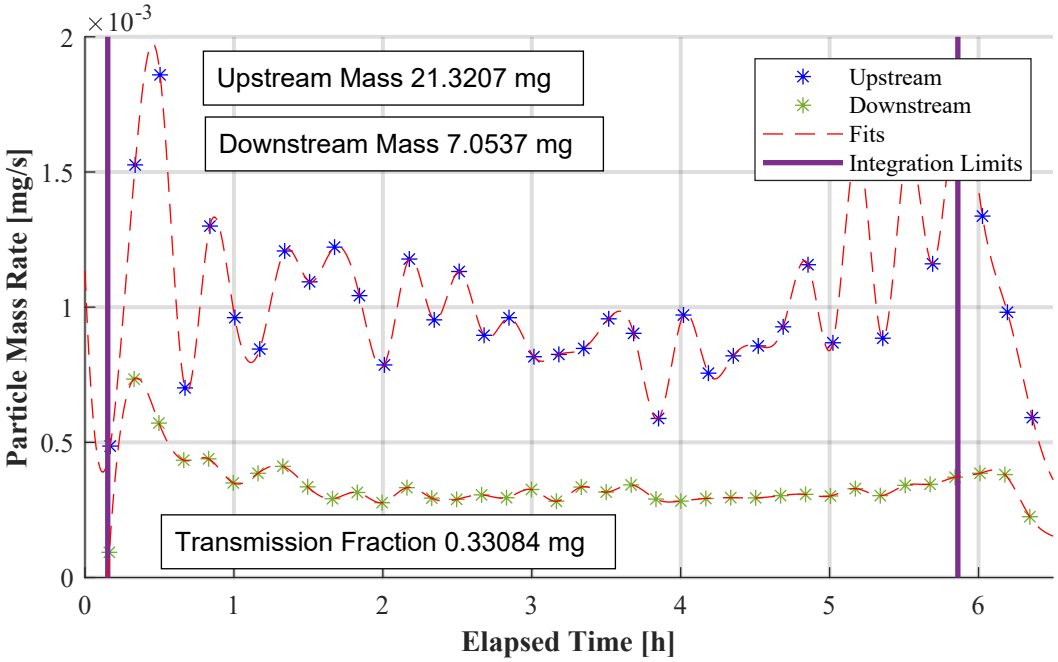

Figure A-6.7 Particle mass rate with spline fits for integration for the air test with active seeding conducted on 07/21/2023 with upstream pressure = 650 kPa.

A.2.4 800 kPa Helium

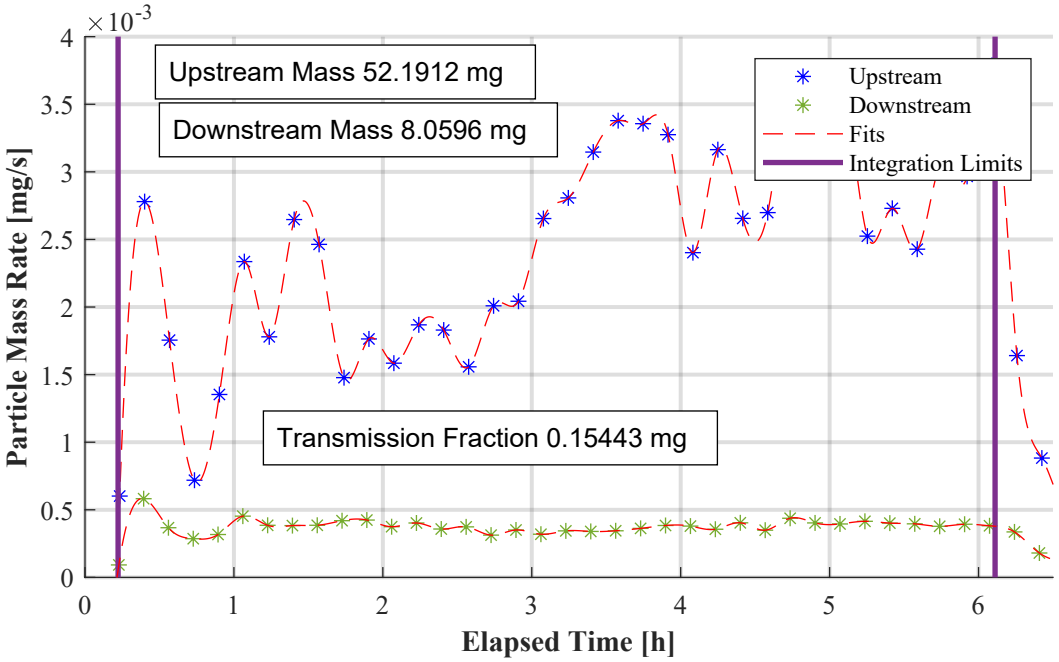

Figure A-6.8 Particle mass rate with spline fits for integration for the air test with active seeding conducted on 07/25/2023 with upstream pressure = 800 kPa.


Sandia National Laboratories